ORIGINAL RESEARCH

Nanohydroxyapatite (nHAp) Doped with Iron Oxide Nanoparticles (IO), miR-21 and miR-124 Under Magnetic Field Conditions Modulates Osteoblast Viability, Reduces Inflammation and Inhibits the Growth of Osteoclast – A Novel Concept for Osteoporosis Treatment: Part 1

Krzysztof Marycz [1,2]
Agnieszka Smieszek [1]
Klaudia Marcinkowska [1]
Mateusz Sikora [1]
Eliza Turlej [1]
Paulina Sobierajska [3]
Adrian Patej [3]
Alina Bienko [4]
Rafal J Wiglusz [3]

[1]The Department of Experimental Biology, The Faculty of Biology and Animal Science, University of Environmental and Life Sciences, Wroclaw, Poland; [2]International Institute of Translational Medicine, Malin, Poland; [3]Institute of Low Temperature and Structure Research, PAS, Wroclaw, Poland; [4]Faculty of Chemistry, University of Wroclaw, Wroclaw, Poland

Correspondence: Krzysztof Marycz
The Department of Experimental Biology, The Faculty of Biology and Animal Science, University of Environmental and Life Sciences Wroclaw, Norwida 27B St, Wroclaw, 50–375, Poland
Tel +48 71 320 5201
Email krzysztof.marycz@upwr.edu.pl

Purpose: Osteoporosis results in a severe decrease in the life quality of many people worldwide. The latest data shows that the number of osteoporotic fractures is becoming an increasing international health service problem. Therefore, a new kind of controllable treatment methods for osteoporotic fractures is extensively desired. For that reason, we have manufactured and evaluated nanohydroxyapatite (nHAp)-based composite co-doped with iron oxide (IO) nanoparticles. The biomaterial was used as a matrix for the controlled delivery of miR-21-5p and miR-124-3p, which have a proven impact on bone cell metabolism.

Methods: The nanocomposite $Ca_5(PO_4)_3OH/Fe_3O_4$ (later called nHAp/IO) was obtained by the wet chemistry method and functionalised with microRNAs (nHAp/IO@miR-21/124). Its physico-chemical characterization was performed using XRPD, FT-IR, SEM-EDS and HRTEM and SAED methods. The modulatory effect of the composite was tested in vitro using murine pre-osteoblasts MC3T3-E1 and pre-osteoclasts 4B12. Moreover, the anti-inflammatory effects of biomaterial were analysed using a model of LPS-treated murine macrophages RAW 264.7. We have analysed the cells' viability, mitochondria membrane potential and oxidative stress under magnetic field (MF+) and without (MF-). Moreover, the results were supplemented with RT-qPCR and Western blot assays to evaluate the expression profile for master regulators of bone metabolism.

Results: The results indicated pro-osteogenic effects of nHAp/IO@miR-21/124 composite enhanced by exposure to MF. The enhanced osteogenesis guided by nHAp/IO@miR-21/124 presence was associated with increased metabolism of progenitor cells and activation of osteogenic markers (*Runx-2, Opn, Coll-1*). Simultaneously, nanocomposite decreased metabolism and differentiation of pre-osteoclastic 4B12 cells accompanied by reduced expression of *CaII* and *Ctsk*. Obtained composite regulated viability of bone progenitor cells and showed immunomodulatory properties inhibiting the expression of inflammatory markers, ie, *TNF-α, iNOs* or *IL-1β*, in LPS-stimulated RAW 264.7 cells.

Conclusion: We have described for the first time a new concept of osteoporosis treatment based on nHAp/IO@miR-21/124 application. Obtained results indicated that fabricated nanocomposite might impact proper regeneration of osteoporotic bone, restoring the balance between osteoblasts and osteoclast.

Keywords: nanocomposites, hydroxyapatite, osteoblasts, osteoclasts, osteoporosis

Introduction

Osteoporosis is a multifactorial disorder strongly associated with reduced bone mass, structural deterioration of bone tissue and mineralization, leading to a high risk of skeletal fractures, including the hip, spine, and wrist. Osteoporosis prevalently affects women, although men are also at high risk of its occurrence.[1] Osteoporosis seems to be a global concern of societies worldwide, especially in well developed and ageing populations.[2] Risk factors for osteoporosis and bone fractures in osteoporotic patients include age (>65 years), genetic predispositions, inactive lifestyle, smoking and low/high BMI index.[3] Moreover, treatment with glucocorticoids, diabetes mellitus type 1 and 2 (T1D and T2D, respectively), rheumatoid arthritis, multiple myeloma or liver associated disorders has been shown as a secondary cause of osteoporosis.[4] As estimated by the National Health Institute (NIH), more than 200 million patients worldwide are affected by osteoporosis. Additionally, the International Osteoporosis Foundation has calculated that 1 in 3 women over the age of 50 and 1 in 5 men will suffer from osteoporosis-related bone fractures in their lives.[5] Osteoporosis results in a severe decrease in life quality and leads to a significant financial burden on the healthcare systems all over the world.[6] Current osteoporosis treatment strategies include applications of anti-resorptive agents, including bisphosphonates, estrogen, selective estrogen receptor modulators (SERMs), and parathyroid hormone (PTH), vitamin D and calcium supplementation.[7,8]

Osteoporosis-related bone fractures belong to the most common consequences of reduced bone mass, as well as deterioration in structural bone tissue formation.[2] Bone fractures, including hip damage, occurring primarily in man, require long-term nursing home care, cause decreased quality of life, social isolation, depression, and in certain cases can even lead to death.[9]

Vertebral fractures become a lion part of osteoporotic related fractures and usually might occur during daily chores without any trauma or fall.[10] Bone fractures that occur spontaneously, called fragility fractures, are predominantly noted in osteoporotic patients. It is also estimated that only in European countries, more than 30% of men will experience an osteoporotic fracture.[10,11] In the course of osteoporosis advantage of bone catabolic over anabolic processes has been shown. Consequently, enhanced bone resorption caused by hyperactivity of osteoclasts is observed, simultaneously with the diminished activity of osteoblasts involved in new bone formation.[12] These processes are regulated in particular by the molecular triad, ie, the receptor activator for nuclear factor κB ligand (RANKL), receptor activator for nuclear factor κB (RANK) and osteoprotegerin (OPG).[13] The deterioration of bone homeostasis at a molecular level is modulated by osteoblasts producing both OPG and RANKL, thus regulating the resorbing activity of osteoclasts activity. The mechanisms mediating proper interplay between osteoblast and osteoclast are critical factors in osteoporosis development. Osteoblasts through the cell to cell contact can affect osteoclast viability, differentiation and apoptosis by activating OPG/RANKL/RANK, LGR4/RANKL/RANK, Ephrin2/ephB4 and Fas/FasL pathways.[12] In turn, osteoclasts can also regulate bone formation via activation of osteoblasts d2 isoform of vacuolar (H+) ATPase V0 domain (Atp6v0d2), complement component 3a, semaphorin 4D or microRNAs, such as miR-214-3p.[12] In the course of osteoporosis, both osteoblasts as well as their stem progenitor cells, are losing their ability to produce extracellular matrix, which finally leads to impairment of bone microstructure.[14] At the same time, osteoclasts involved in bone resorption and modulation of this process are strongly activated, leading to reduced bone density and initiates bone fractures.[9] Thus, the factors that could regulate and coordinate the crosstalk between osteoblast-osteoclasts activity are strongly required to improve the regeneration of bone fractures. Recently, many factors have been shown to promote bone healing via stimulation of osteoblasts activity, including apatites.[15,16]

Nanohydroxyapatite (nHAp) is used for bone substitution and has been shown to promote bone regeneration by modulating viability, proliferative activity and metabolic activity of osteoblasts and their progenitors.[17] Hydroxyapatite is an essential component of vertebrate bone mineral. Fabrication of nHAP and its composites under controlled conditions gives the potential for a multitude of applications, for example, as platforms for drug and bioactive molecules delivery.[16,18,19]

Previous studies published by our group showed that nHAp promotes osteoblasts survival through modulation of expression of common transcripts involved in cell viability, including *BCL-2, BAX, P21* and *P53*.[20] The nHAp matrices have been shown to improve mineralization of

extracellular matrix activating transcripts at mRNA level, including RUNX2, which is the master regulator of differentiation of bone cells and RANKL-OPG axis. However, nHAp also promotes osteoclasts activity, which seems undesirable, especially considering the design of biomaterials for the regeneration of osteoporotic bone fractures.[21] For that reason, many strategies have been proposed to improve bone regeneration, including co-doping of nHAp by various agents, including iron oxide nanoparticles (IOs).[22] Due to the antimicrobial properties of IOs noted against pathogenic bacteria and fungi, their application as factors for guided regeneration of disturbed tissue is highly desirable. Moreover, IOs can be synthesized via the green route, which allows obtaining materials having not only a strong antibacterial activity but also photocatalytic properties, which expands their potential biomedical application.[22]

We have recently shown that nHAp doped with IOs after exposition to the magnetic field promotes the expression of osteogenic markers in osteoblasts through integrin alpha-3 (INTa-3) activation, simultaneously inhibiting osteoclasts activity.[23] The nHAp/IOs composites reduced tartrate-resistant acid phosphatase activity (TRAP) and cathepsin K – two major regulators of osteoclasts metabolism. Moreover, we showed that nHAp doped with IOs could trigger apoptosis in osteoclasts via activation of BAX-p21-p53 and CASP-9 axis. The combination of both nHAp and IOs under magnetic field condition influenced osteoblast precursors (MC3T3-E1), activating the expression of transcripts coding osteopontin (OPN), bone morphogenetic protein −2 (BMP-2), collagen type 1 (COL1A1) as well as alkaline phosphatase (ALP) – all factors crucial for bone regeneration and remodelling.[23] The combination of nHAp and IOs also brings additional advantages since IOs allow their trucking to use magnetic resonance imaging (MRI) and deliver particular agents, including genes, growth factors or miRNA.[24,25]

Recently, miRNAs have been shown to play a critical function as post-transcriptional regulators of bone metabolism and a fundamental role as modulators of osteoblasts-osteoclasts axis activity.[26] MicroRNAs are actively involved in the regulation of both post-transcriptional processes of bones remodelling. Therefore, miRNAs known as critical agents influencing bone homeostasis seem to be promising therapeutic factors that modulate bone formation and resorption. Previously performed studies showed that microRNA-21 (miR-21) is particularly involved in osteogenic differentiation of bone marrow-derived stromal mesenchymal stem progenitor cells (BM-MSCs), and regulates downstream targets, including Sprouty 1 (Spry1) and Sprouty 2 (Spry2).[27] The miR-21 molecule is also involved in preventing bone loss through inhibition of osteoclasts activity and targeting programmed cell death protein 4 (PDCD4), despite the existence of RANKL.[28]

In turn, microRNA-124 (miR-124) has been shown to play a critical role in the regulation of osteoclastogenesis in BM-MSCs through suppressing NFATc1 expression.[29] Moreover, the overexpression of NFATc1 prevents the inhibitory effect of miR-124 on osteoclastogenesis. Finally, miR-124 affects the viability and proliferative potential of osteoclast precursors, which shed a bright light on its application as a so-called osteoclast "blocker".[30]

The study's objective was to develop a novel nHAp-based platform co-doped with iron oxide (IO) for the controlled delivery of microRNA that regulates the activity of bone-forming and bone-resorbing cells. This study is the first and foremost communication revealing the third generation's conceptual material for the guided regeneration of osteoporotic bone. The innovation of the proposed dual-targeting system relies on applying nHAp/IO as a platform delivering therapeutic miRNA, ie, miR-21 and miR-124 released after triggering with the magnetic field. The fabricated scaffold, ie, nHAp+IO with a combination of miR-21/124, actively improved osteoblasts activity, increasing proliferative potential as well as viability through activation of BCL-2 transcript. The functionality of the scaffold was evidenced by increased osteogenesis of osteoblast precursors. Moreover, we revealed that nHAp/IO@miR-21/124 application inhibits osteoclasts activity and has immunomodulatory properties, thus might become a promising therapeutic approach for osteoporosis treatment, facilitating osteoblast-osteoclast coupling.

Materials and Methods
Synthesis of Iron Oxide Nanoparticles (IO)

The wet chemical co-precipitation process has been applied to obtain magnetic nanoparticles. The following reagents were used: KOH (Chempur, Piekary Slaskie, Poland, pure p.a.), KNO_3 (Chempur, Piekary Slaskie, Poland, <99%) and $FeSO_4 \cdot 7H_2O$ (Chempur, Piekary Slaskie, Poland, <99.5%). The hot water solutions of 0.4329 g (4.28 mmol) KOH, 1.4415 g (25.69 mmol) KNO_3 and 3.5712 g (12.85 mmol) $FeSO_4 \cdot 7H_2O$ were

prepared. Afterwards, the KNO_3 and KOH solutions were added dropwise to dissolved $FeSO_4 \cdot 7H_2O$ and further stirred at 90 °C for 10 minutes. The resulting black precipitate was magnetically separated from the by-products, washed with deionised water to obtain a neutral pH and dried at 70 °C for 24 hours.

Synthesis of Nanohydroxyapatite/Iron Oxide Composite (nHAp/IO)

Fabrication of nHAp/IO composite was done by using a microwave-stimulated hydrothermal method. 0.3000 g (1.3 mmol) of the obtained iron oxide (Fe_3O_4) and 1.0647 g (8.06 mmol, 3-fold excess relative to the calcium ion concentration) diammonium hydrogen phosphate (($NH_4)_2HPO_4$, Acros Organics, Geel, Belgium 98+%) were mixed and sonicated in 20 mL of deionised water for 15 minutes. Then, 5 mL of ammonia (25%) was added to the mixture to obtain an alkaline environment. Afterwards, the water solutions of 1.0577 g (4.48 mmol) calcium nitrate (Ca($NO_3)_2$, Sigma-Aldrich, Steinheim, Germany >99%) and 0.1721 g (0.08 mmol) citric acid ($C_6H_8O_7$, Alfa Aesar, Karlsruhe, Germany, 99+%) were added. After sonification for 10 min the dispersion was transferred to Teflon vessel and put in a microwave reactor (Magnum II, ERTEC-Poland, Wrocław, Poland) under the pressure of 20–30 atm and at 200 °C for 90 minutes. Afterwards, the obtained powder was washed with deionised water to obtain neutral pH and further dried at 70 °C for 24 h.

Characterisation of Fabricated nHAp/IO

The X-Ray Powder Diffraction (XRPD) patterns were recorded in a 2θ range of 5–100 with X'Pert Pro PANalytical X-ray diffractometer (Malvern Panalytical Ltd, Malvern, UK) (Cu Kα1: 1.54060 Å) to confirm the structure of obtained composite. To calculate the cell parameters and contribution of both phases in nHAp/IO the Rietveld refinement was used.[31] The resulted structure was confirmed by mid-IR (4000–400 cm^{-1} with 4 cm^{-1} spectral resolution) spectrum collected in KBr pellets using the Nicolet iS50 Fourier Transform Infrared Spectroscopy (Thermo Scientific, Waltham, MA, USA) spectrometer equipped with Automated Beamsplitter exchange system (iS50 ABX containing DLaTGS KBr detector), Thermo Scientific Polaris[TM] and HeNe laser as an IR radiation source. The morphology and elemental analysis were carried out using the scanning electron microscope FEI Nova NanoSEM 230 (FEI Company, Hillsboro, OR, USA)

equipped with an EDS spectrometer (EDAX Pegasus XM4, AMETEK Materials Analysis Division, Mahwah, NJ USA) and operating acceleration voltage in the range 3.0–15 kV and spot 2.5–3.0. High-resolution transmission electron microscopy (HRTEM) images and selected area electron diffraction (SAED) patterns were investigate using a Philips CM-20 SuperTwin (Philips, Amsterdam, Netherlands) microscope operating at 160 kV. The average particles size was determined through direct measurement of 60 particles in the HRTEM images using ImageJ software (National Institutes of Health, Wisconsin, USA).

Variable temperature (1.8–300 K) direct current (DC) magnetic susceptibility measurements under an applied field of B = 0.01 T and variable – field (0–5 T) magnetization measurements at temperatures 2 and 300 K were carried out with SQUID MPMS magnetometer (Quantum Design, California, USA). The magnetic susceptibility data were corrected for the diamagnetism of the constituent atoms and the sample holder. DC measurements were carried out by crushing the crystals and restraining the sample to prevent any displacement due to its magnetic anisotropy.

Functionalization of Obtained nHAp/IO by the miR21/124

The surface of nanocomposite was functionalized by miRNA (MISSION ® miRNA Mimics of miR-21 and miR-124; Sigma Aldrich, Munich, Germany) in complex with poly-L-lysine (Merck/Sigma-Aldrich, Munich, Germany). The complex was prepared in molecular biology-Grade water and mixed with 0.1 g of nHAp/IO. The final concentration of miRNA in the experimental condition was equal to 50 nM. This mixture was incubated for 24 h at a temperature of 40 °C. Afterwards, the modified nanocomposite was centrifuged and dried at 30 °C per 24 h. The spectrophotometric method has been applied to determine the modifier content. 1 mg/g of miRNA were incorporated into nHAp/IO@miRNA bio-composite.

Evaluation of nHAp/IO Cytocompatibility
Cell Culture

The murine osteoblast precursor cell line (MC3T3-E1) and murine monocyte-macrophage cell line (RAW 264.7) were obtained from EACC (European Collection of Authenticated Cell Cultures, Merck/Sigma-Aldrich, Munich, Germany). Pre-osteoclastic murine cell line (4B12) was a kind gift from Shigeru Amano

(Department of Oral Biology and Tissue Engineering, Meikai University School of Dentistry in Japan).

The pre-osteoblast MC3T3-E1 cell line was cultured in a complete growth medium, ie, MEM-α without the addition of ascorbic acid (Minimum Essential Media Alpha, Gibco, Scotland, UK) supplemented with 10% FBS (Fetal Bovine Serum; Merck/Sigma-Aldrich, Munich, Germany) named later CGM_{MC3T3}. In turn, 4B12 cell line was cultured in MEM-α supplemented with 10% FBS and additionally with 30% of CSCM, which is a cell-conditioned medium obtained from calvaria-derived stromal cells as it was described by Amano et al[32]. The complete growth medium for 4B12 pre-osteoclasts was named later CGM_{4B12}. Moreover, RAW 264.7 cell line was cultured in a complete growth medium ($CGM_{RAW264.7}$) consisting of DMEM medium (Dulbecco's Modified Eagle Medium, with 10% FBS and 4500mg/L glucose (Merck/Sigma-Aldrich, Munich, Germany). The growth media were not supplemented by the antibiotics.

All cultures were maintained in CO_2 incubator at constant conditions (37°C, 5% CO_2, 95% humidity). The medium was replaced every 2–3 days. The trypsinization protocols of MC3T3 and 4B12 cell lines were described in detail previously.[33] Passage of macrophage cells line was carried out by dislodging cells from the flask with a cell scraper when the culture reached 80% of confluence. Pre-osteoblasts used for experiments were at passage 45 (p45), and osteoclast precursors were at passage 40 (p40).

The Experimental Cultures

Cell lines propagated with or without the addition of biomaterials were exposed to the magnetic field (MF+) for 15 minutes daily. As a negative control, cell lines culturing without exposure to the magnetic field were used (MF-). The system for magnetic field generation was described in detail by Marycz et al[34]. The magnetic field stimulation system was installed in CO_2 incubator and established to 0.2 T.

Pre-osteoblasts were inoculated onto 24-well plastic plates (Greiner, Biokom, Janki, Polska) at the density of 3×10^4 cells/well and maintained in 500 μL of CGM_{MC3T3}. Pre-osteoclasts were inoculated onto 24-well plastic plates at the density of 6×10^4 cells/well and cultured in 500 μL of CGM_{4B12}.

Mouse monocyte-macrophages cells, ie, RAW 264.7 were inoculated in 24-well plastic plates at the density of 3×10^5 cells/well and maintained in 500 μL $CGM_{RAW264.7}$. Subsequently, lipopolysaccharide from *Pseudomonas*

aeruginosa (LPS, Merck/Sigma-Aldrich, Munich, Germany) at a concentration of 1 μg/mL was added to the experimental culture. After 6 h of incubation, the medium with LPS was removed and replaced with a new fresh portion of CGM supplemented with nHAp/IO@miR21/124. The experiment last four days, cultures were maintained in an incubator at standard growth conditions (37°C, 5% CO_2, 95% humidity) with daily exposition to the magnetic field for 15 min.

Evaluation of Cells' Viability and Mitochondrial Membrane Depolarization

The cells' viability and mitochondrial membrane potential were investigated using Muse™ Mitopotential Assay Kit (Merck/Sigma-Aldrich, Munich, Germany). The protocol was performed accordingly to manufacturers' instruction, and it was shown in our previous studies.[35,36] After incubations with provided reagents, the samples were analysed using Muse™ Cell Analyzer (Merck/Sigma-Aldrich, Munich, Germany). Each measurement was performed in triplicate. Additionally, the MTS assay (Abcam, Cambridge, UK) was performed using a well-known protocol performed according to the method described before.[35]

Mitochondria Network Visualization

The visualization of mitochondria in cells was performed using MitoRed staining kit, obtained from Merck/Sigma-Aldrich (Munich, Germany), according to the manufacturers' protocol and protocols described elsewhere.[37] Cultures were counterstained with phalloidin solution in PBS (1:800) for 40 min at 37°C (Atto 488, Merck/Sigma-Aldrich, Munich, Germany). The Mounting Medium with 4′,6-diamidino-2-phenylindole, ie, DAPI (Thermo Fisher Scientific, Waltham, MA, USA), was used to visualize the cell nuclei and closed the microscopic glass slides. Cells were analyzed under a confocal microscope (Leica TCS SPE, Leica Microsystems, Wetzlar, Germany). The photographs were captured under 630× magnification. Moreover, the stained mitochondria network's intensity was analyzed using Fiji New ImageJ with Colour Pixel Counter plugin version 1.52n developed by Wayne Rasband from National Institutes of Health, USA. Each measurement was performed in triplicates.

Evaluation of Reactive Oxygen Species Releasing

The oxidative stress activation was evaluated in the murine monocyte-macrophage cell line, ie, RAW 264.7. The assay was performed using Muse™ Oxidative Stress commercial

Kit (Merck/Sigma-Aldrich, Munich, Germany). The protocol of reaction was performed according to the manufacturer's instruction. The measurements were performed using Muse[TM] Cell Analyzer (Merck/Sigma-Aldrich, Munich, Germany). Each measurement was performed in triplicate.

Osteogenic Differentiation Determination

Osteogenic differentiation evaluation was performed using mice pre-osteoblast cell line, ie, MC3T3-E1. Briefly, the pre-osteoblasts were inoculated onto 6-well plastic plates (Greiner, Biokom, Janki, Polska) at the density of 1.5×10^5 cells/well and maintained in 2 mL of CGM_{MC3T3} complete medium. The osteogenic conditions and medium composition were described in detail previously.[33] The osteogenesis was carried out for 14 days. Cells were maintained in an incubator at standard conditions (37°C, 5% CO2, 95% humidity), and experimental groups were additionally exposed to MF every day for 15 minutes within these days. After differentiation, the cells were fixed with 4% of paraformaldehyde or collected for further analysis.

Detection of calcium deposits was performed using Alizarin Red S (Merck/Sigma-Aldrich, Munich, Germany). The protocol of extracellular matrix staining, methods of documentation and analysis of the obtained results were performed as described previously.[38]

The protein expression of intracellularly accumulated RUNX-2 and OPN was evaluated by the Western Blot technique. The procedure was carried out using the conditions described previously in detail.[36,39] The concentration of protein level loaded per well was equal to 20 μg. The primary antibody for RUNX-2 (F-2: sc-390351, Santa Cruz Biotechnology, Dallas, Texas, USA) detection was diluted at the ratio of 1:100 and for OPN (ab8448, Abcam, Cambridge, UK) at the ratio of 1:1000. The documentation was performed as described previously.[33]

The visualization of the RUNX-2 and OPN protein in cells was also verified using confocal fluorescence microscopy. Secondary antibodies conjugated with fluorochrome were diluted at concentration equal 1:1000. Antibodies used for the analysis were Anti-Mouse IgG – Atto 594 antibody produced in goat (Sigma, 76085) and anti-Rabbit IgG – Atto 594 antibody produced in goat (Sigma, 77671). The images were captured using a confocal microscope at magnification 630× (Leica TCS SPE, Leica Microsystems, Wetzlar, Germany). Obtained photographs were analysed by ImageJ software version 1.52n, developed by Wayne Rasband, National Institutes of Health, USA.

RT-qPCR Detection of Gene Expression

The evaluation of mRNAs and non-protein-coding RNAs transcript levels was performed using RT-qPCR technique. The procedures were performed accordingly to our previous studies.[33,35,36] Briefly, to isolate the RNA, cultures were homogenized by the addition of Extrazol® (Blirt DNA, Gdańsk, Poland). The purity and the quantity of obtained RNA were measured by a spectrophotometer at 260 and 280 nm wavelength (Epoch, BioTek Instruments, Vermont, USA). The PrecisionDNAse Kit (Primerdesign, BLIRT S. A., Gdańsk, Poland) and Tetro cDNA Synthesis Kit (Bioline Reagents Limited, London, UK) were used according to the manufacturer's protocol in order to digest the gDNA and synthesize cDNA from 800 ng of RNA. The digestion and reverse transcription were performed in T100 Thermal Cycler (BioRad, Hercules, CA, USA). Furthermore, the evaluation of small non-coding RNA levels was performed using the Mir-X[TM] miRNA First-Strand Synthesis Kit (Takara Clontech Laboratories, Mountain View, CA, USA) according to the protocol provided with reagents. The qPCR reaction was performed using SensiFAST SYBR Green®and Fluorescein Kit from Bioline Reagents Ltd., London, UK. For the analysis, CFX Connect Real-Time PCR Detection System (Bio-Rad, Hercules, CA, USA) was applied. The reactions were performed in triplicates. The genes expression were calculated according to the RQ_{MAX} algorithm using Bio-Rad CFX Maestro. The mRNA transcripts were calculated in relation to the housekeeping gene, ie, *Gapdh* (glyceraldehyde 3-phosphatehydrogenase), while miRNA transcripts were normalized to snU6 gene. The primers (Sigma Aldrich, Munich, Germany) are listed in Table 1S (Supplementary material).

Statistical Analysis

Obtained results are presented as the mean with standard deviation (±SD), derived from at least three technical repetitions. Statistics comparison was performed using t-Student test or One-way analysis of variance with Dunnett's post hoc test. The calculation was made using GraphPad Software (Prism 8.20, San Diego, CA, USA). Differences with a probability of $p < 0.05$ were considered significant.

Results

Structure and Morphological Properties of the Obtained nHAp/IO

The obtained nHAp/IO was verified by comparing detected positions of the diffraction peaks with the data relating to the

A

B

C
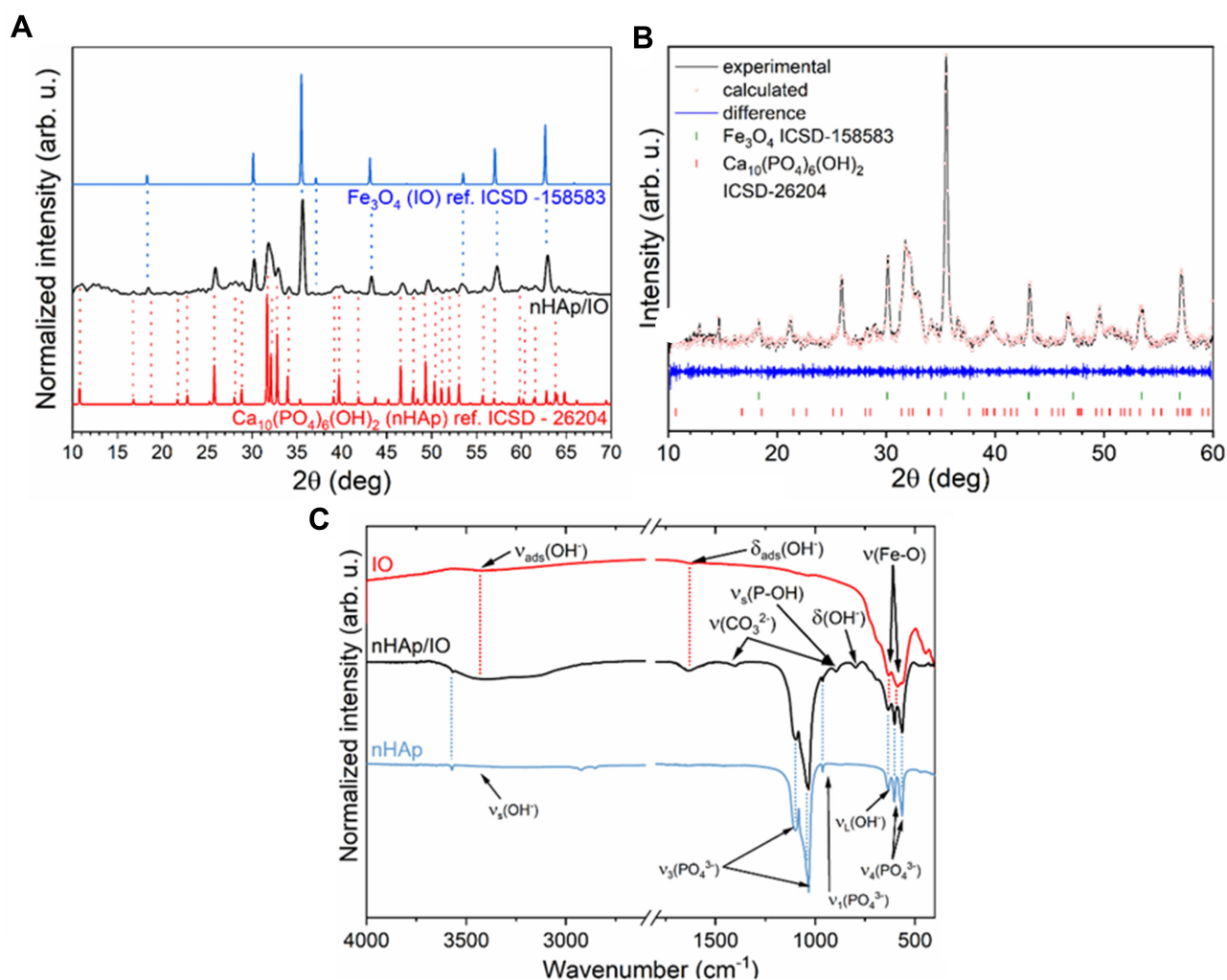
Figure 1 XRD pattern of the obtained nHAp/IO together with the corresponding references (**A**). Result of the Rietveld analysis (black line– XRPD pattern; red points— fitted diffraction; blue—differential pattern; red and green—positions of reference phase peaks) (**B**). FT-IR spectrum of the obtained nHAp/IO (black line) with the indication of characteristic bands originating from IO (red line) and nHAp (blue line) (**C**).

Inorganic Crystal Structure Database standards (ICSD-26204 for hydroxyapatite[40] and ICSD-158583 for magnetite[41]). The peaks (see Figure 1A) at 2θ equal to 18.4°, 30.2°, 35.6°, 37.0°, 43.1°, 53.4°, 57.2°, 62.7° has been ascribed to cubic inverse spinel structure, which crystallizes in orthorhombic $Fd\bar{3}m$ space group.[42] Whereas the most characteristic peaks belonging to the hexagonal hydroxyapatite structure ($P6_3/m$ space group) were found at 16.8°, 25.8°, 28.0°, 28.89°, 39.0°, 39.9°, 55.69° and in the 2θ range from 31.6° to 33.9°, as well as from 46.6° to 53.0°.

Table 1 Unit Cell Parameters (a, c), Crystal Cell Volume (V), as Well as a Refined Factor (Rw) for the Nanocomposite $Ca_5(PO_4)_3OH/Fe_3O_4$

Cell Parameters						Phase		
	Hydroxyapatite $Ca_5(PO_4)_3OH$			Magnetite Fe_3O_4		$Ca_5(PO_4)_3OH$ (%)	Fe_3O_4(%)	R_w
Sample	a (Å)	c (Å)	V (Å³)	a (Å)	V (Å³)			
s. c.	9.424(4)	6.879(4)	529.09(54)	8.394(1)	591.43(21)	–	–	–
Composite	9.416(9)	6.866(8)	527.35(24)	8.377(2)	587.89(08)	68.01	31.99	1.01

Notes: $Ca_5(PO_4)_3OH$ – ICSD 26204, Fe_3O_4 – ICSD 158583.
Abbreviations: s. c. – single crystal reference data.
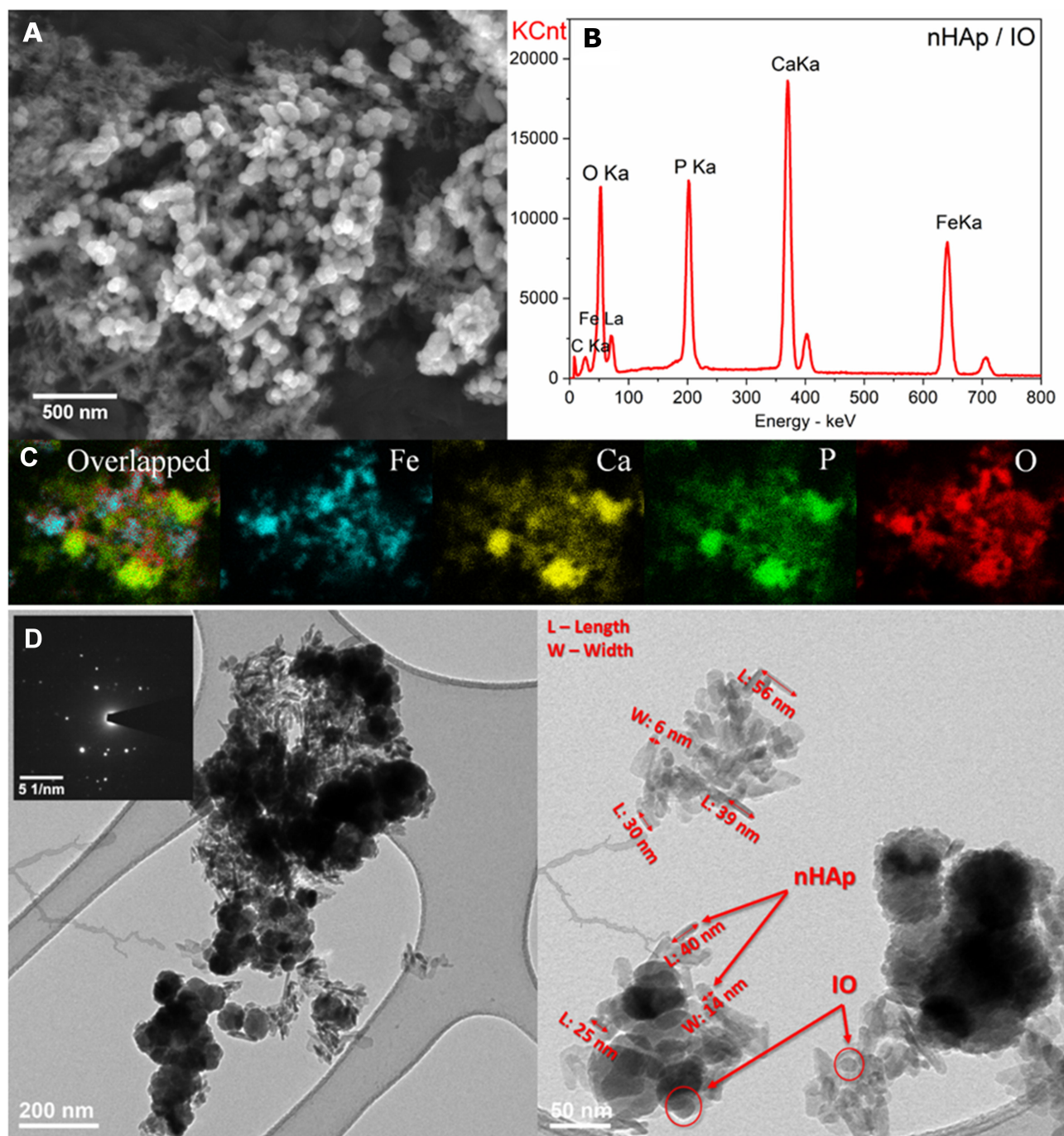
Figure 2 SEM image (**A**), EDS spectrum (**B**), SEM-EDS elemental maps (**C**) and TEM with SAED (inset) images (**D**) of the obtained nHAp/IO.

The FT-IR spectrum recorded for the obtained nHAp/IO composite has been shown in c. The spectrum consists of the vibrational bands characteristic for phosphate (PO_4^{3-}) and hydroxyl (OH^-) groups belonging to nHAp. The bands detected at 565, 603 cm^{-1} correspond to the triply degenerate v_4 bending of O–P–O bonds vibration. The peak at 960 cm^{-1} belongs to the symmetric non-degenerate v_1

stretching vibrations of phosphate groups, while the modes at 1031 and 1092 cm^{-1} identify the antisymmetric triply degenerate v_3 stretching vibrations of PO_4^{3-} group.[43] The presence of band at 1404 and 869 cm^{-1} indicates the C–O vibrations of adsorbed CO_2 from air or substitution of PO_4^{3-} with CO_3^{2-} groups.[44,45] The typical for nHAp bands at 632 and 3572 cm^{-1} represent librational modes ($v_L(OH^-)$) and

stretching vibrations ($v_S(OH^-)$) of hydroxyl groups, respectively.[43,46,47] Whereas the broad stretching (3800–2800 cm^{-1}) and bending (1637 cm^{-1}) bands can be assigned to adsorbed water molecules on the nanoparticle surface.[48,49] The bands occur at 580 cm^{-1} and 634 cm^{-1} can be attributed to the stretching vibration of Fe–O bond derived from iron oxide.[48,50,51] Both peaks are overlapped by absorption peaks assigned to nHAp (Figure 1C).

The cell parameters and contribution of these two phases in the final composite were calculated using Rietveld analysis. Figure 1B shows a good relationship between the composite XRPD pattern and the theoretical fits of both phases, indicating the validity of the Rietveld refinement as illustrated by the close to zero differences in the intensity scale in the line (Y$_{Obs}$ − Y$_{Calc}$). The quality of structural refinement was checked by R_w value. The results have been gathered in Table 1. The phase content was estimated to be 68.01% for nHAp and 31.99% for IO. The calculated cell parameters (a, c, V) of both components are in good agreement with theoretical values. However, a contraction of the unit cell volume is observed for both hydroxyapatite and iron oxide. This observation is probably related to the nano-dimension of the composite.

Scanning Electron Microscopy together with Energy Dispersive X-ray spectroscopy (SEM-EDS) was used to examine the composition of the obtained nHAp/IO and its atomic distribution (Figure 2A–C). The composite contains Ca, P, O and Fe elements in the amount of 25.46, 11.48, 32.48 and 36.56 Wt%, respectively. The estimated Ca/P molar ratio (1.72) is close to the theoretical value equals to 1.67. The elemental maps (Figure 2C) have

shown that iron ions are separately distributed from other ions belonging to hydroxyapatite as well as both phases, IO and nHAp, have a tendency towards mutual agglomeration. Moreover, to estimate the size of the obtained hydroxyapatite and magnetite as well as see how the particles interact with each other, Scanning (SEM) and Transmission (TEM) Electron Microscopy images were collected. As shown, nHAp particles possess rods-shape with an average size of approximately 25–56 nm x 4–16 nm. In contrast, iron oxide particles have a spherical-like morphology in nanometric size. Furthermore, the Selected Area Electron Diffraction (SAED) image shows well-developed spotty rings confirming that the sample is poly-nanocrystalline (Figure 2D).

Magnetic Properties of the Obtained nHAp/IO

As reported in the literature, the magnetic order in the cubic spinel system of magnetite is mainly due to a superexchange interaction mechanism occurring between the metal ions in the A and B sites in spinel lattice. The magnetic properties of the composite material were examined by means of superconducting quantum interference device (SQUID) within the temperature range of 1.8–300 K (Figure 3A) and a magnetic field of 0–5T (Figure 3B).

The zero-field cooling curve of examine sample are almost flat in the temperature range 25–150 K and displays a hump at T=25 K. Above 150 K this curve decreases rapidly with temperature suggesting superparamagnetic behavior with a little interaction among the particles. The sharp fall of ZFC magnetization at T_f is
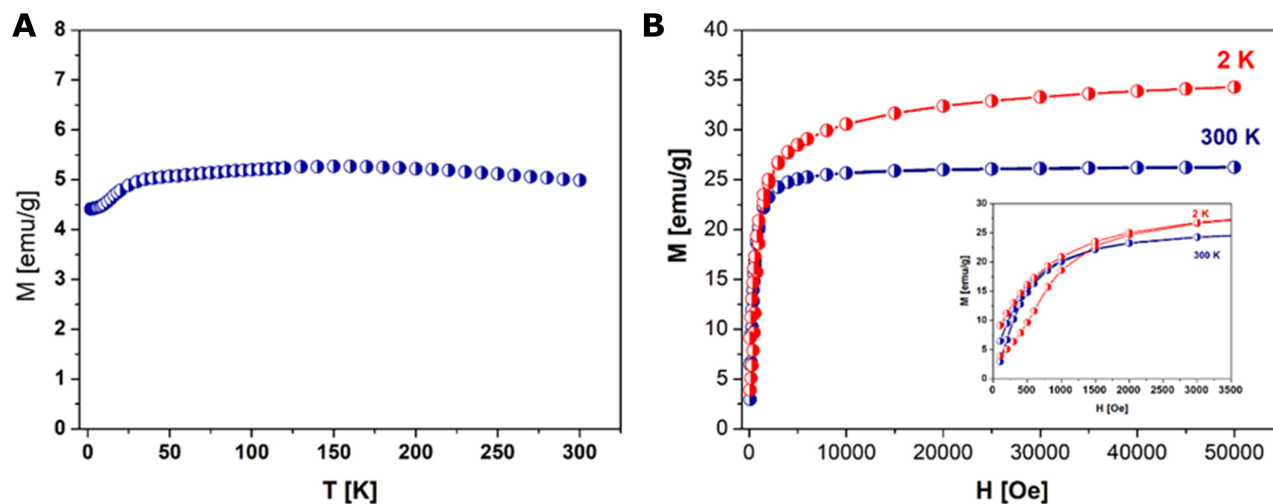

Figure 3 (**A**) Temperature (T) dependence of magnetization (M) at 100 Oe for nHAp/IO. (**B**) Field (H) dependence of magnetization (M) of nHAp/IO at 300 K and 2 K.
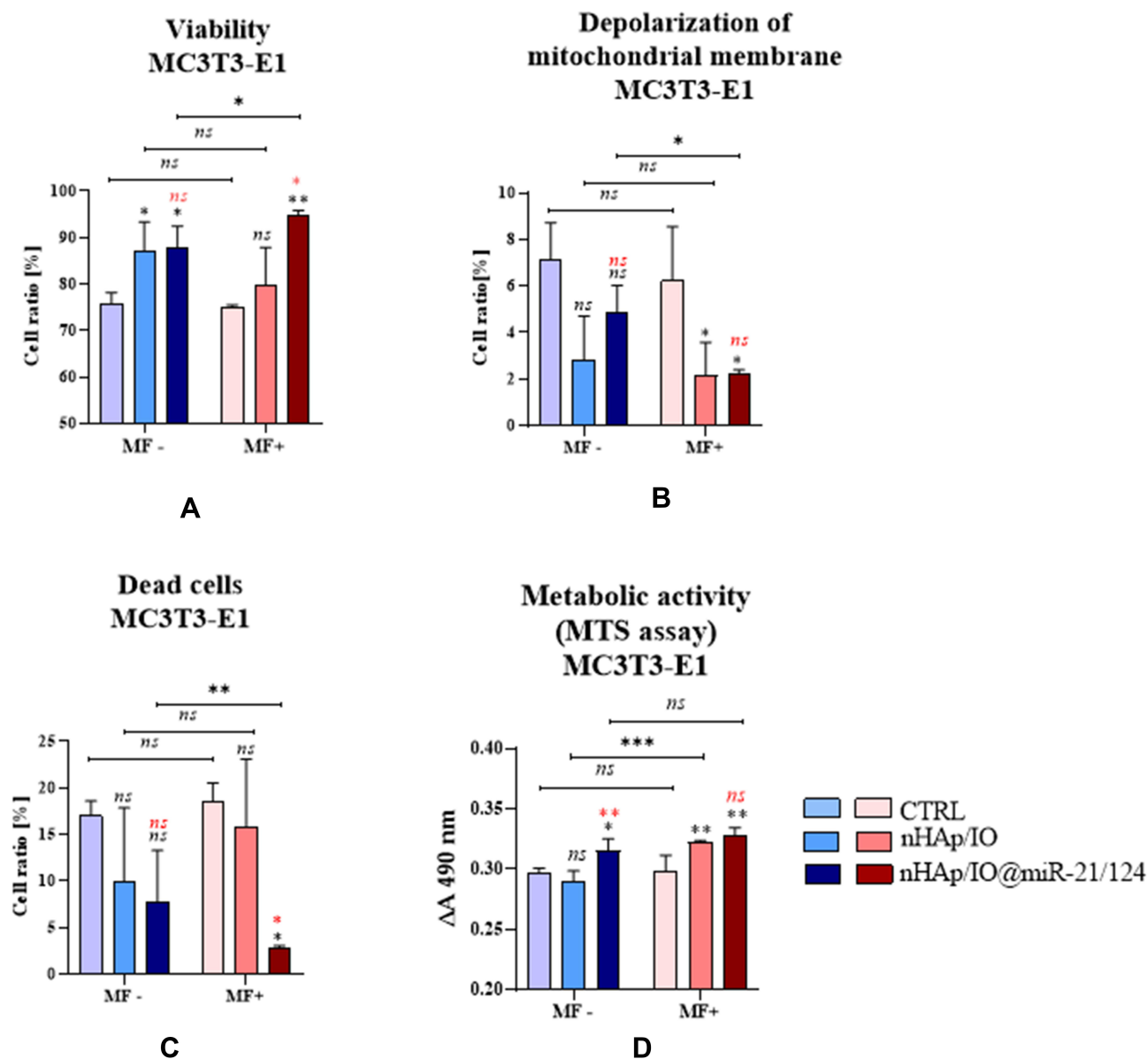
Figure 4 The impact of the nanocomposites alone and in combination with the miR21/124 in MF conditions on the mitochondrial potential of MC3T3-E1 cells. The results of comparative analysis, including cells with high mitochondrial membrane potential/viable (**A**), with the depolarised mitochondrial membrane (**B**) and dead (**C**). The metabolic activity was determined based on mitochondrial dehydrogenase activity (**D**). Significant differences are indicated as follows (*p<0,005, **p<0,001 and ***p<0,001) and non-significant are marked as ns. The comparisons between groups are marked with brackets. The black symbols refer to the differences between CTRL and nHAp/IO groups, while red symbols are for nHAp/IO and nHAp/IO@miR-21/124 groups.

indicative of the typical co-operative freezing (spin glasslike) behavior of strongly interacting particles in a frustrated magnetic system.[52,53] Some useful information about the magnetic response of both samples give hysteresis loops graph shown in Figure 3B recorded at 300 and 2 K, respectively. These figures show a nonlinear variation in magnetization as a function of a magnetic field at both temperatures. At 300 K, the coercivity (18.5 Oe) and remanence values (2.1 EMU/g) are not discernible, indicating a superparamagnetic behavior, while at 2 K the value of coercivity (160 Oe) and remanence (7.5 EMU/g) showing a ferrimagnetic behavior. The observed value of saturation magnetization (Ms) at 2 T and 300 K was 34.1 and 26.6 emu/g, respectively. The smaller magnetizations than their respective bulk value 92 emu/g for magnetite[54] are likely due to the mass of the composite material, some diamagnetic contribution from the hydroxyapatite shell and tendency towards mutual agglomeration.[55,56]
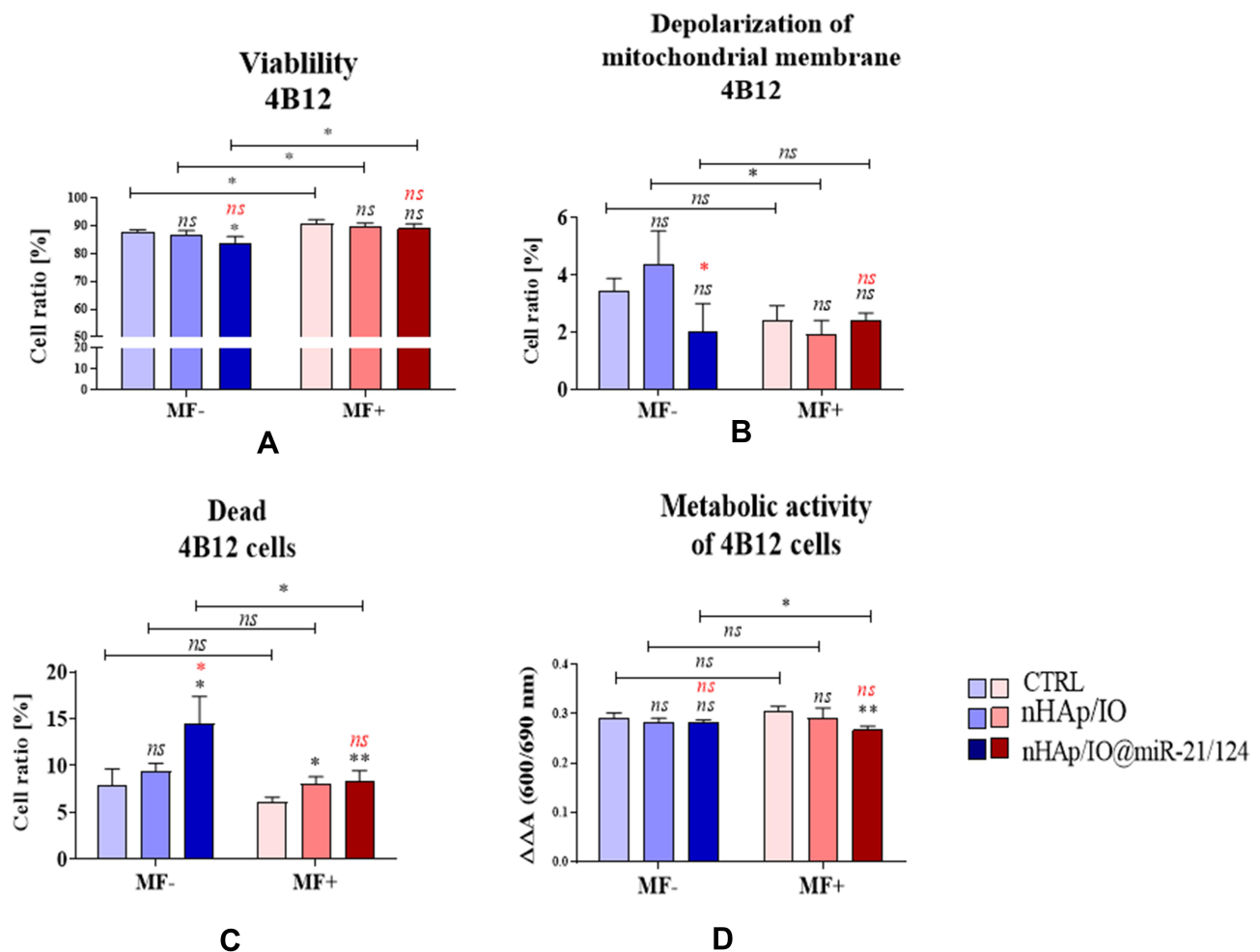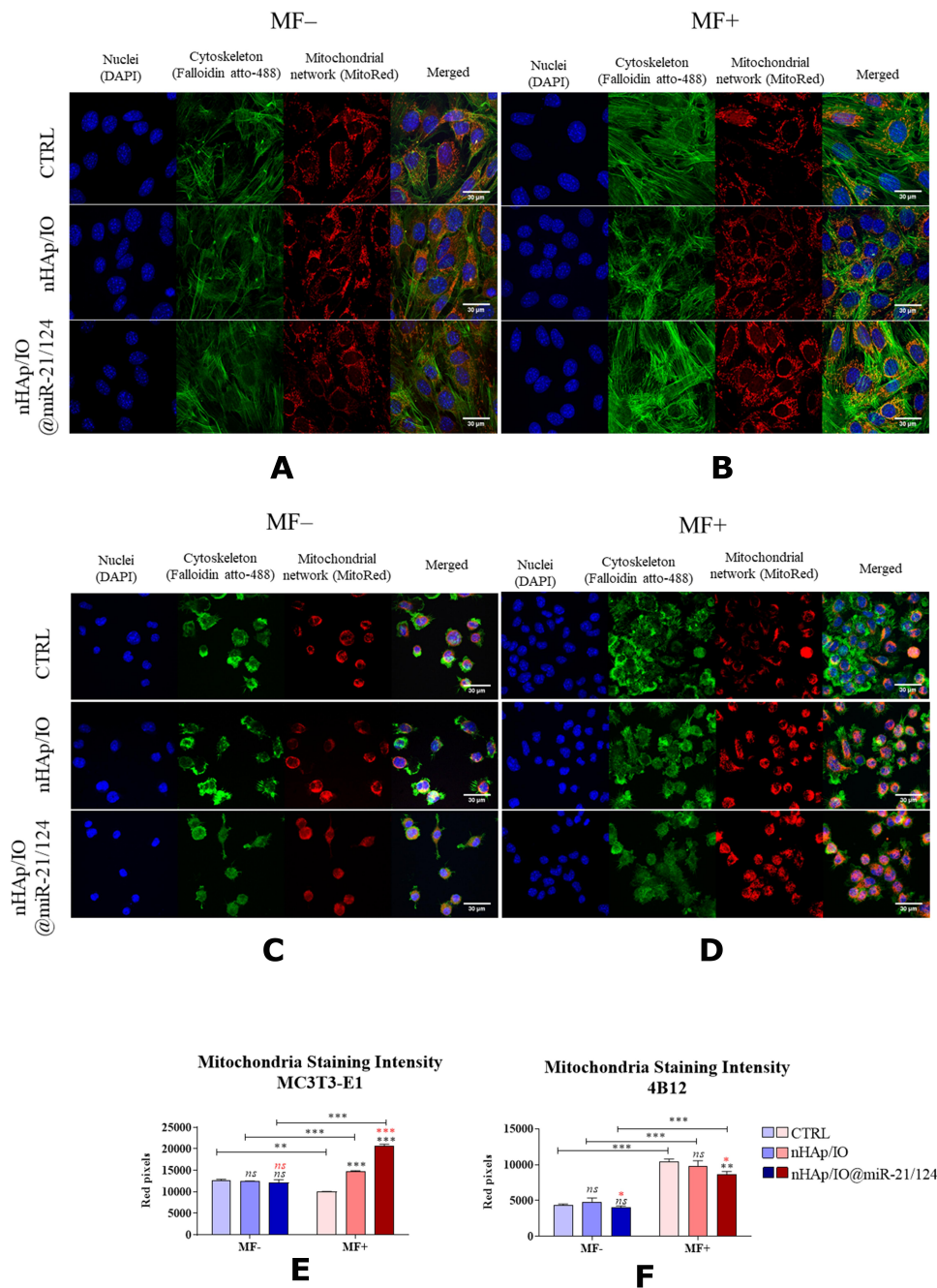
Figure 5 The impact of the nanocomposites alone and in combination with the miR21/124 in MF conditions on the mitochondrial potential of 4B12 cells. The results of comparative analysis, including cells with high mitochondrial membrane potential/viable (**A**), with the depolarised mitochondrial membrane (**B**) and dead (**C**). The metabolic activity was determined based on mitochondrial dehydrogenase activity (**D**). Significant differences are indicated as follows (*p<0,005 and **p<0,001) and non-significant are marked as ns. The comparisons between groups are marked with brackets. The black symbols refer to the differences between CTRL and nHAp/IO groups, while red symbols are for nHAp/IO and nHAp/IO@miR-21/124 groups.

Viability and Mitochondrial Membrane Potential are Modulated in Pre-Osteoblast and Pre-Osteoclast by the Presence of Biomaterial and Magnetic Field

The viability of precursors of bone cells was determined based on the impact of the combination of the nHAp/IO@miR21/124 on the mitochondrial membrane polarisation (Figure 4A–C) and its metabolism (Figure 4D). The representative dot plots showing distribution of pre-osteoblast based on mitochondrial membrane potential, were shown in Supplementary Information (Figure 1S). The analysis revealed that pre-osteoblasts derived from MC3T3-E1 cell line cultured with the addition of nHAp/IO are characterised by increased viability independently

of the magnetic field influence (Figure 4B). The significant difference in the viability of cells cultured without biomaterials and with nHAp/IO biomaterials was observed only in those maintained without magnetic field (MF-). Simultaneously, MC3T3-E1 cultured under MF+ condition with the addition of nHAp/IO showed a significant decrease of mitochondria membrane depolarisation and increased metabolic activity (Figure 4B and D). Additionally, the effect of nHAp/IO functionalisation with miRNAs (nHAp/IO@miR21/124) was significantly enhanced in cultures propagated under magnetic field (MF+). The cultures were distinguished by increased viability coupled with decreased mitochondrial membrane depolarisation and reduced percentage of dead cells (Figure 4A–C). Moreover, nHAp/IO combined with miRNAs, improved the metabolic activity of cells

MF−

MF+

A **B**

MF−

MF+

C **D**

E **F**

Figure 6 The impact of the nanocomposites alone and in combination with the miR21/124 in MF conditions on the morphology, growth pattern, mitochondrial network development and mitochondria staining intensity in MC3T3-E1 (**A, B, E**) and 4B12 cell line (**C, D, F**). Significant differences are indicated as follows (*p<0,005, **p<0,001 and ***p<0,001) and non-significant are marked as ns. The comparisons between groups are marked with brackets. The black symbols refer to the differences between CTRL and nHAp/IO groups, while red symbols are for nHAp/IO and nHAp/IO@miR-21/124 groups.

(Figure 4D). Nevertheless, in comparison to nHAp/IO the significant effect was noted only in cultures propagated without MF.

The analysis of 4B12 pre-osteoclast viability showed that MF stimulation significantly improved mitochondria membrane potential (Figure 5). Simultaneously, we have noted that in 4B12 cell line culture, maintained under MF, both nHAp/IO and nHAp/IO@miR21/124, increased the

percentage of necrotic cells (Figure 5C). We have also demonstrated that the viability of 4B12 decreases in cultures with nHAp/IO@miR-21/124 in MF-condition (Figure 5C), which was accompanied by lowered mitochondrial membrane potential and increased occurrence of necrotic (dead) cells (Figure 5A and B). The representative dot plots obtained in cytometric-based assay were shown in Supplementary Information (Figure 2S). The
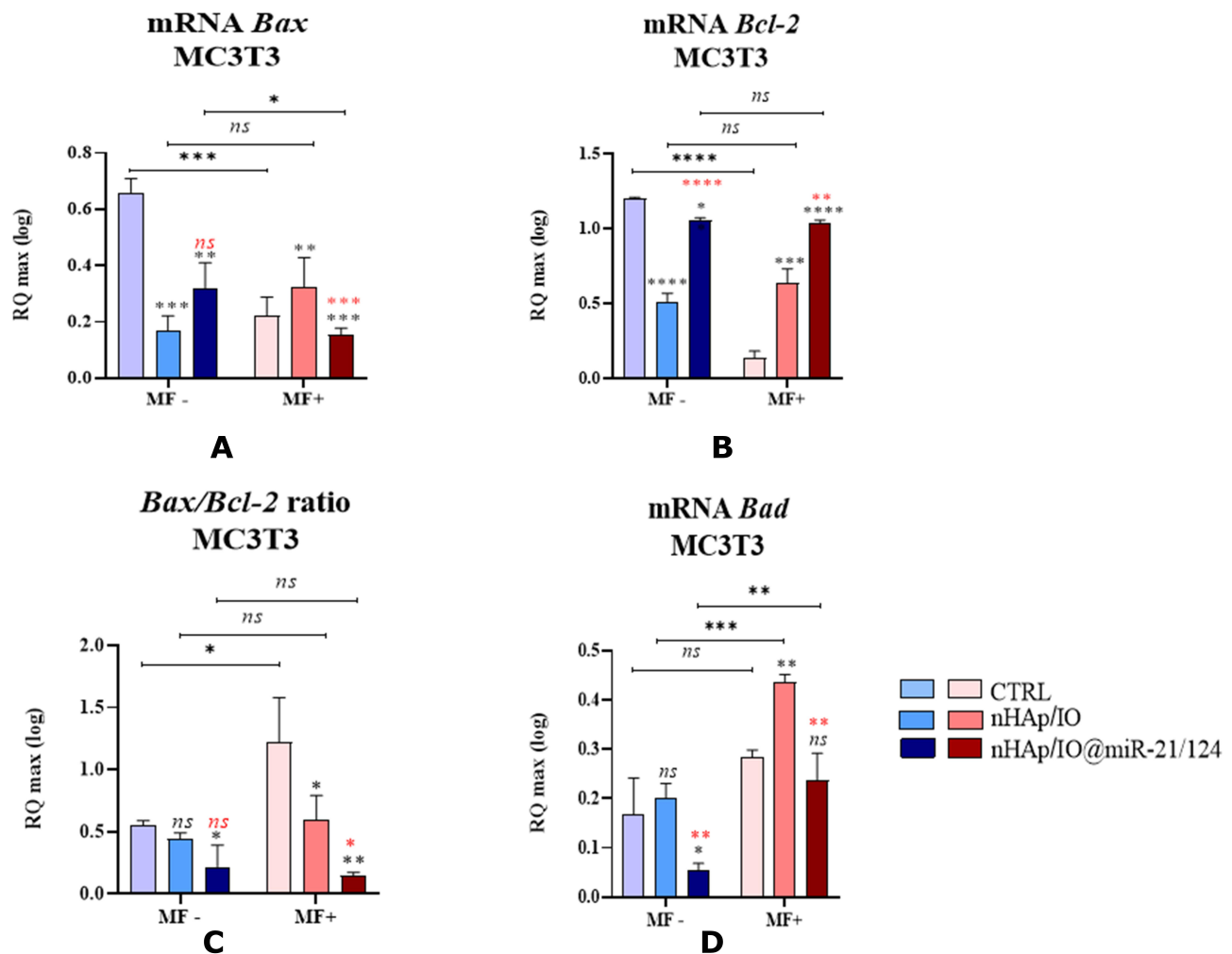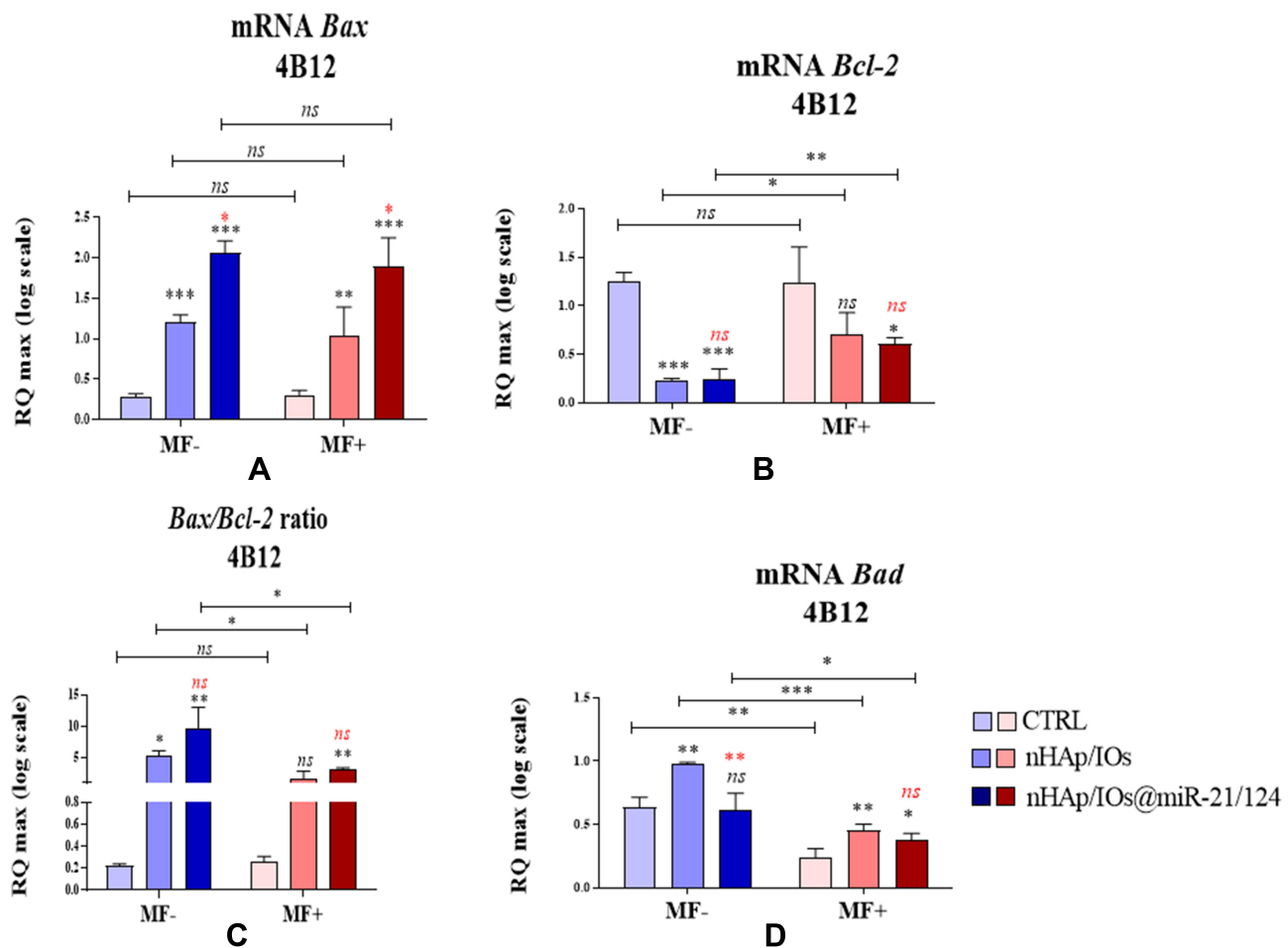
Figure 7 The impact of the nanocomposites alone and in combination with the miR21/124 on the expression on *Bax* (**A**), *Bcl-2* (**B**),*Bad* (**D**) and ratio *Bax/Bcl-2* (**C**) associated with apoptosis in MC3T3-E1 cell line. Significant differences are indicated as follows (*p<0,005, **p<0,001,***p<0,001, and ****p<0.0001) and non-significant are marked as ns. The black symbols refer to the differences between CTRL and nHAp/IO groups, while red symbols are for nHAp/IO and nHAp/IO@miR-21/124 groups.

analysis of metabolic activity measured in the MTS assay indicated that the biomaterial does not influence on 4B12 cell line cultured in MF- conditions (Figure 5D). Nevertheless, the nHAp/IO@miR-21/124 biomaterial influenced on the lowered metabolic activity of 4B12 pre-osteoclasts in cultures under magnetic field (Figure 5D).

The effect of biomaterials on morphology, growth pattern of cultures and development of the mitochondrial network is presented in Figure 6. We have shown that obtained biomaterials, both native nHAp/IO and functionalised with miRs, did not significantly influence MC3T3-E1 morphology in MF-conditions. In all evaluated experimental conditions, the MC3T3-E1 maintained a proper fibroblast-like phenotype and formed a dense monolayer (Figure 6A and B). However, under MF (MF

+), the growth pattern of cultures was more complex and expanded, associated with the well-developed actin cytoskeleton. Additionally, the mitochondria activity was evaluated based on the fluorescence intensity of the mitoRed dye, confirming the improved activity of MC3T3-E1 cultures treated with obtained biomaterials (Figure 6E). The results are consistent with the analysis of mitochondrial membrane potential and confirmed lowered modest depolarisation of mitochondria in MC3T3-E1 cultures with biomaterials.

In turn, the growth pattern of the pre-osteoclastic cell line 4B12 was altered in response to the tested biomaterials and MF stimulation. The density of the 4B12 cell line in cultures propagated under MF increased, evidenced by the increased number of cells nuclei (Figure 6C and D). The tested biomaterials decreased confluence of 4B12 and affected their

Figure 8 The impact of the nanocomposites alone and in combination with the miR21/124 on the expression on *Bax* (**A**), *Bcl-2* (**B**),*Bad* (**D**) and ratio *Bax/Bcl-2* (**C**) associated with apoptosis in MC3T3-E1 cell line. Significant differences are indicated as follows (*p<0,005, **p<0,001 and ***p<0,001) and non-significant are marked as ns. The comparisons between groups are marked with brackets. The black symbols refer to the differences between CTRL and nHAp/IO groups, while red symbols are for nHAp/IO and nHAp/IO@miR-21/124 groups.

intracellular interactions, causing a reduction of filopodia and podosomes formation. The analysis of staining intensity confirmed these observations (Figure 6F).

The pro-survival effect of biomaterials towards the MC3T3-E1 cells is evidenced by the expression profile of markers associated with apoptosis. The Bax/Bcl-2 ratio indicates that nHAp/IO and nHAp/IO@miR-21/124 exert a significant anti-apoptotic effect on osteoblast precursors in cultures maintained under the MF (Figure 7A–C).

The anti-apoptotic effect of nHAp/IO@miR-21/124 is also emphasised by the lowered expression of Bad transcripts, regardless of MF presence (Figure 7D). On the other hand, cells cultured in the presence of nHAp/IO under MF conditions showed increased accumulation of mRNA for Bad (Figure 7D).

The analysis of mRNA levels for Bax and Bcl-2, as well as their ratio performed for 4B12 pre-osteoclasts,

confirmed the fact that biomaterials may increase the death occurrence of bone-resorbing cells. The pro-apoptotic marker Bax was significantly increased in 4B12 cultured with the addition of biomaterials, while anti-apoptotic Bcl-2 was decreased, regardless of the magnetic field influence (Figure 8A and B). Moreover, the functionalisation of nHAp/IO with the combination of miR-21/124 significantly affected Bax transcript levels. The profile of Bax/Bcl-2 ratio confirms the observation made using cytometric analysis and confocal imaging. The decreased Bax/Bcl-2 ratio was observed in cultures under a magnetic field, indicating that the stimulation may promote the viability of pre-osteoclasts (Figure 8C). Moreover, this pattern confirms the expression profile of pro-apoptotic Bad. The mRNA levels for Bad in all tested culture conditions decreased after magnetic field stimulation. Nevertheless, under MF Bad transcript levels determined
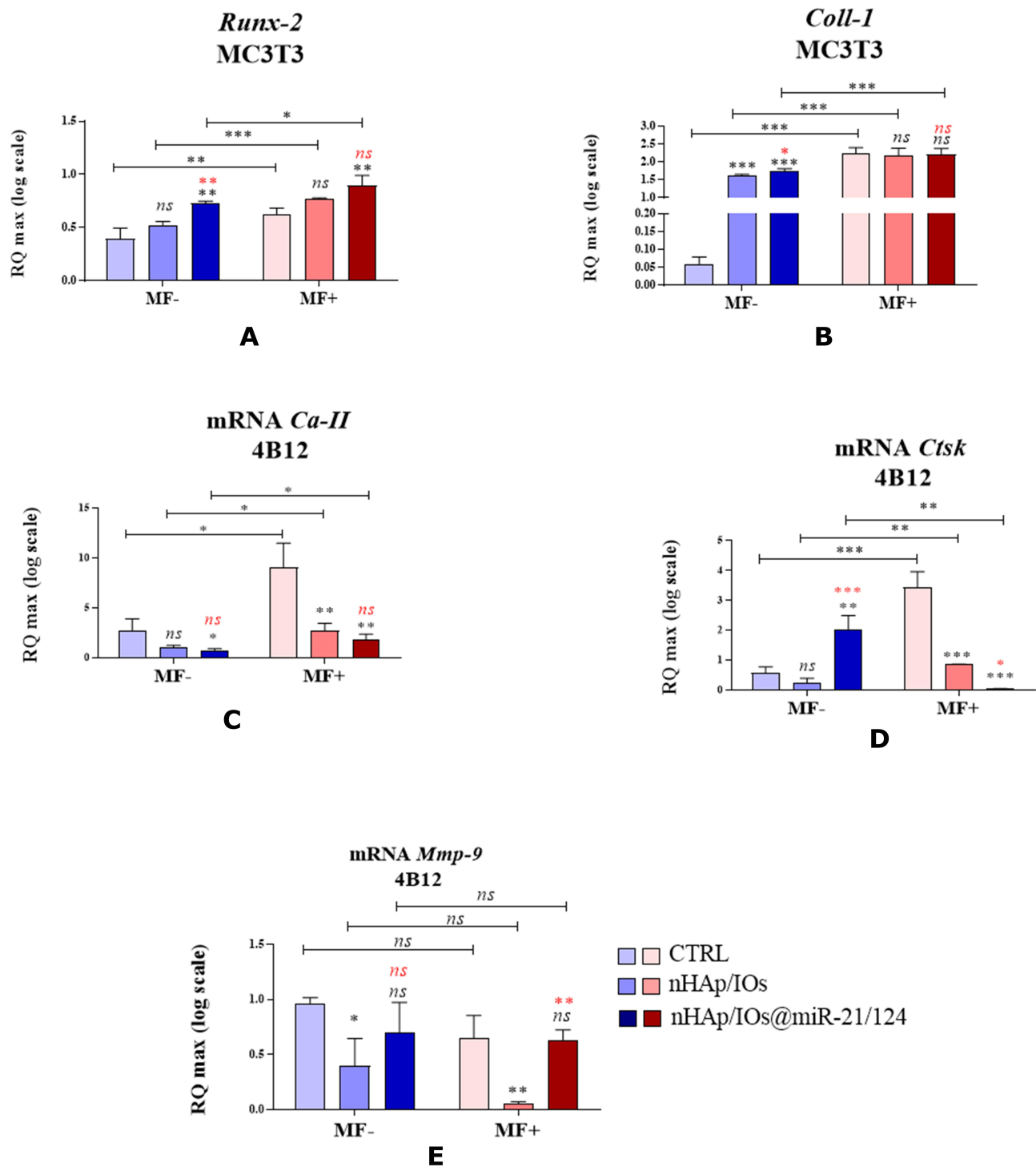
Figure 9 The impact of the nanocomposites alone and in combination with the miR21/124 in condition of MF on the expression of *Runx-2* (**A**), *Coll-1* (**B**), *Ca II* (**C**), *Ctsk* (**D**), *Mmp-9* (**E**) genes associated with bone formation and resorption in MC3T3-E1 and 4B12 cell line. Significant differences are indicated as follows (*p<0,005, **p<0,001 and ***p<0,001) and non-significant are marked as ns. The comparisons between groups are marked with brackets. The black symbols refer to the differences between CTRL and nHAp/IO groups, while red symbols are for nHAp/IO and nHAp/IO@miR-21/124 groups.

in 4B12 experimental cultures, ie, with biomaterials, are significantly increased compared to control cultures. This observation proves the pro-apoptotic effect of the tested constructs toward pre-osteoclast (Figure 8D).

In order to determine the influence of the nHAp/IO and nHAp/IO@miR-21/124 on phenotype changes of bone-formation and cells resorption, we have established mRNA levels for markers essential during
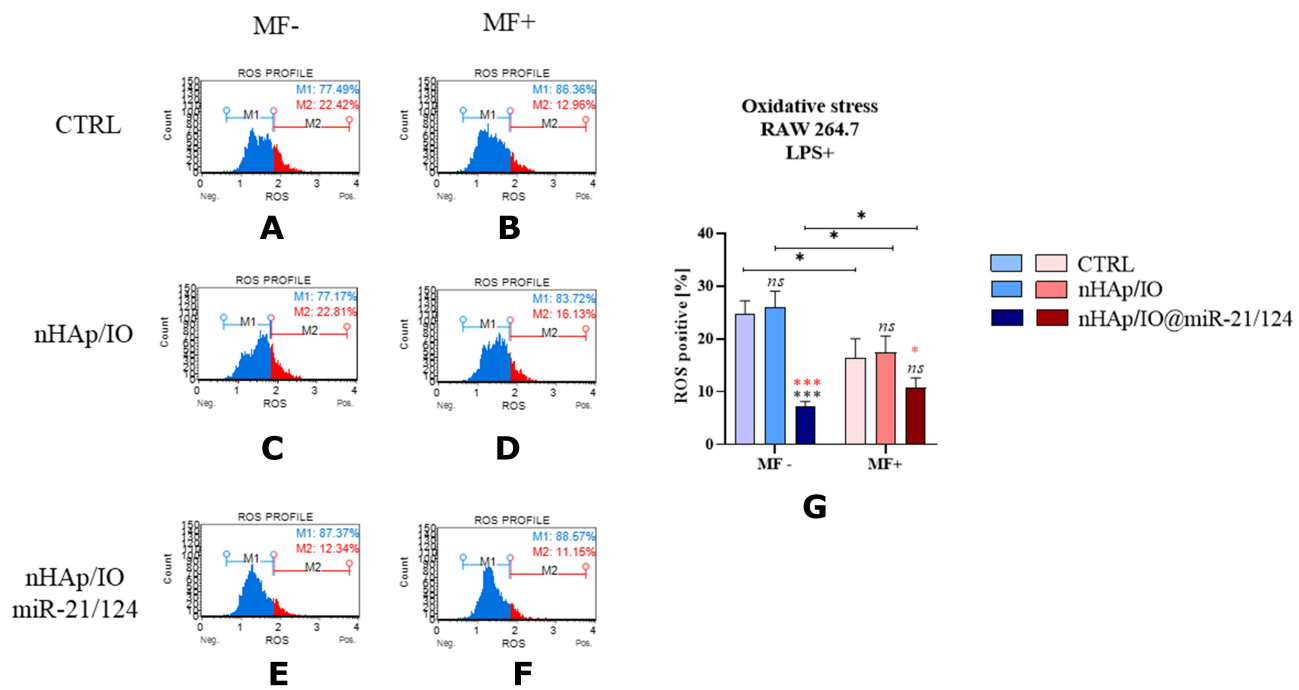
Figure 10 The impact of the nanocomposites alone and functionalized with miR21/124 cultured without magnetic filed influenced (MF-) and under the magnetic influence (MF+) on oxidative status of RAW 264.7 cells. The intracellular accumulation of reactive oxygen species (ROS) was measured in all experimental conditions (**A–F**), and comparative analysis was performed (**G**). The gating strategy included population ROS negative cells (blue part of histogram) and ROS positive cells (red part of the histogram). Significant differences are indicated as follows (*p<0,005 and ***p<0,001) and non-significant are marked as ns. The comparisons between groups are marked with brackets. The black symbols refer to the differences between CTRL and nHAp/IO groups, while red symbols are for nHAp/IO and nHAp/IO@miR-21/124 groups.

osteoblastogenesis and osteoclastogenesis. Thus, we have determined the mRNA levels for runt-related transcription factor 2 (*Runx-2*) and collagen type I (*Coll-1*) in MC3T3-E1 cultures, while carbonic anhydrase II (*CaII*), cathepsin K (*Ctsk*), and matrix metalloproteinase (*Mmp-9*) in cultures of 4B12 pre-osteoblast (Figure 9A–E). The results showed that obtained biomaterials trigger the osteoblast markers expression, regardless of magnetic field presence. Significantly increased expression of *Runx-2* and *Coll-1* has been noted in MC3T3-E1 cell line propagated without MF (Figure 9A and B). We observed that the presence of miR21/miR124 improved the accumulation of *Runx-2* and *Coll-1* transcripts. The mRNA expression for *Coll-1* was significantly increased under MF stimulation, but comparative analysis revealed no differences between experimental and control samples.

Further analysis indicated that obtained biomaterials might exert selective potential in terms of the differentiation of bone cells. The MF alone seemed to improve the expression of *CaII* and *Ctsk*, important factors regulating the differentiation of osteoclasts. However, we have noted that transcript levels for *CaII* are decreased in 4B12 cells in response to biomaterials presence

(Figure 9C and D). Moreover, the functionalisation of nHAp/IO with miRNAs improved the bioactivity of obtained composites. Pre-osteoclasts cultured with nHAp/IO@miR-21/124 showed significantly lowered expression of *Ctsk* under magnetic field (Figure 9D). The expression pattern of *Mmp-9* transcripts determined in 4B12 cells was not affected by magnetic field stimulation. However, in cell lines cultures with the addition of nHAp/IO we noted significantly decreased levels of mRNA for *Mmp-9*, opposite to the accumulation of *Mmp-9* increased after functionalisation of biomaterials with miRNAs (Figure 9E).

The immunomodulatory properties of obtained biomaterials were determined using mouse monocyte-macrophage cell line RAW 264.7, treated with lipopolysaccharide (LPS+). Moreover, intracellular accumulation of reactive oxygen species (ROS) is induced by LPS affecting oxidative status of the cells and their viability. Thus, firstly we have measured LPS-mediated production of ROS. The analysis showed that only nHAp/IO@miR-21/124 decreases the (Figure 10A–G). This phenomenon was significantly evidenced, both under and without the influence of a magnetic field.
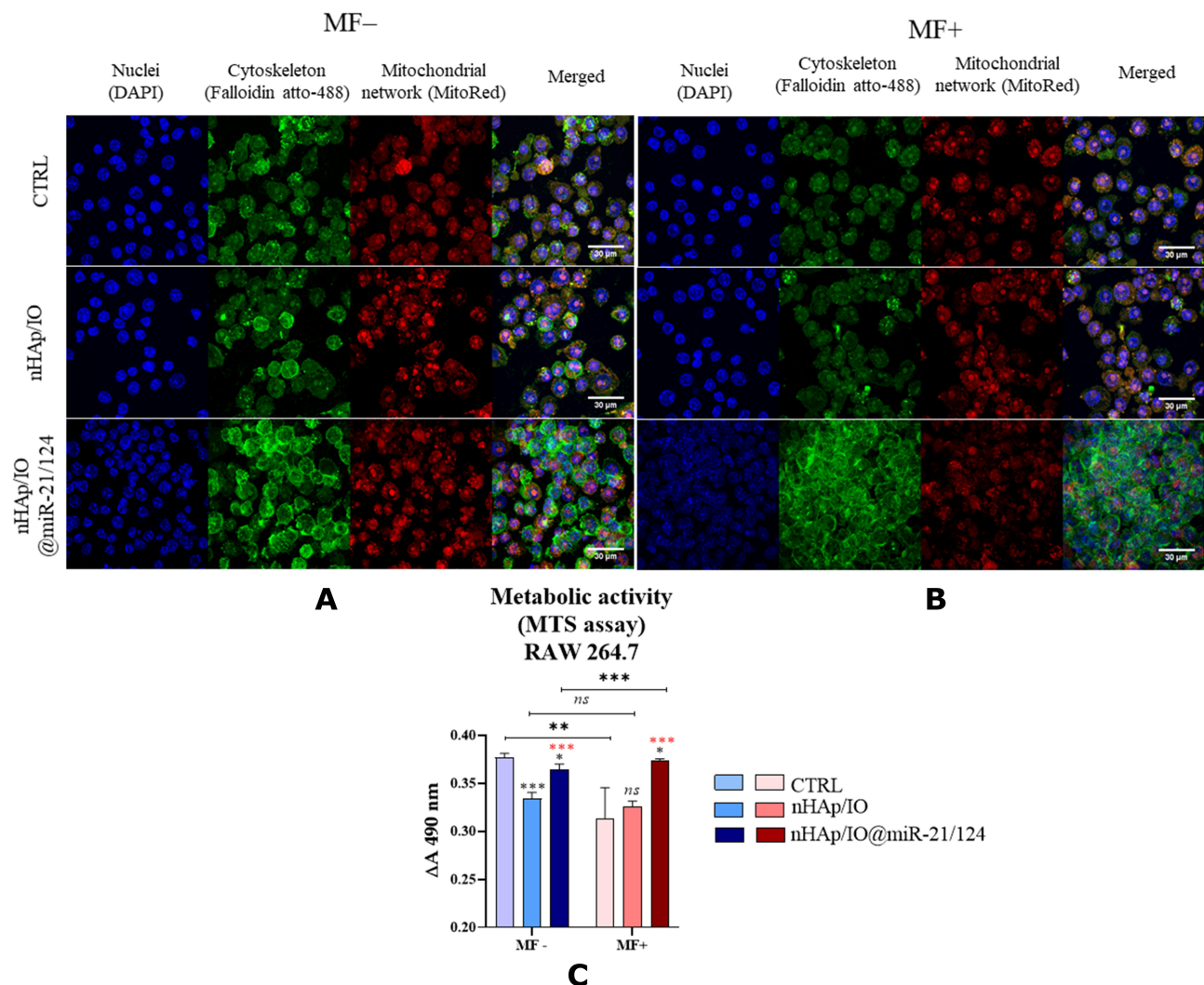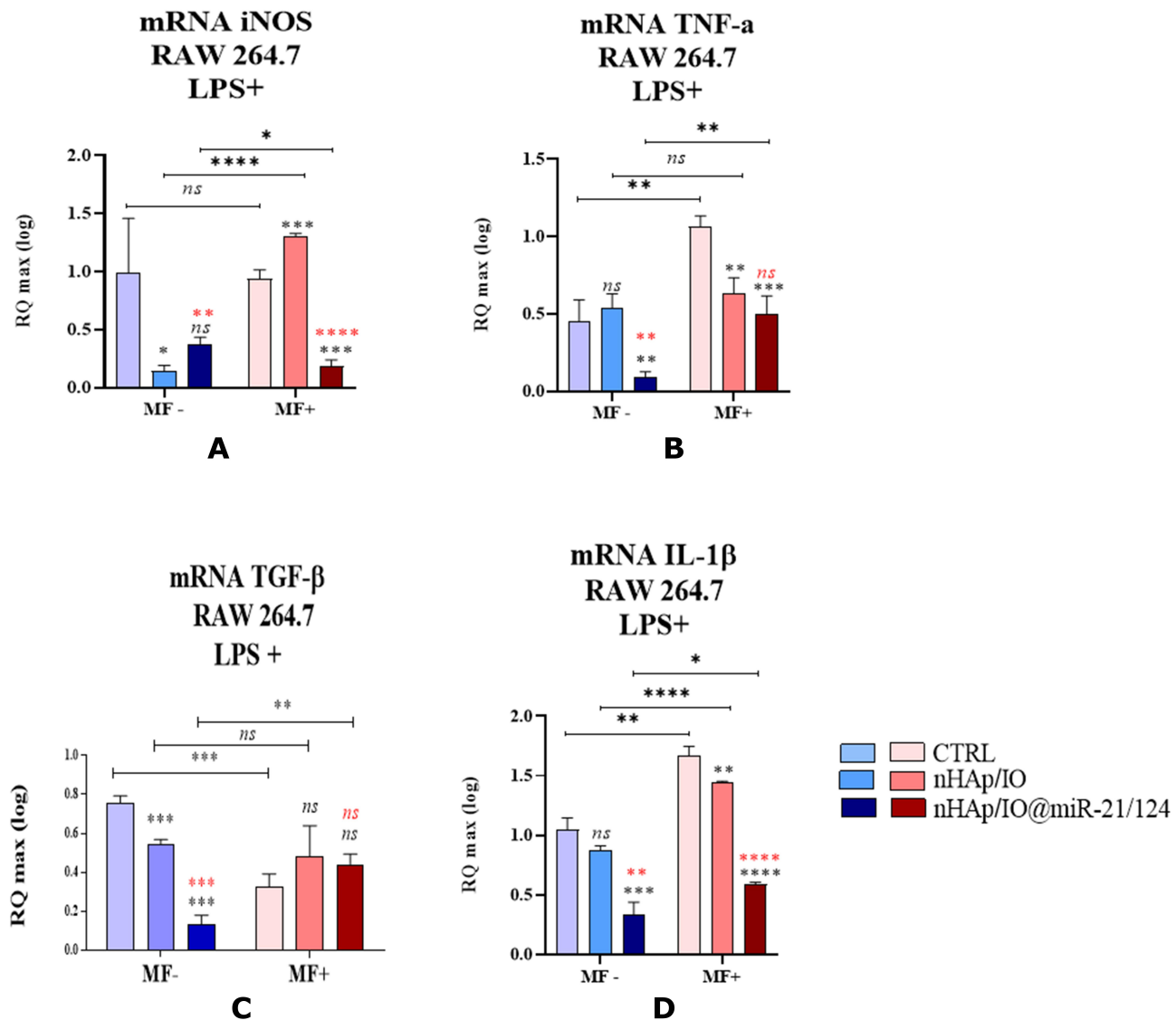
Figure 11 The impact of the nanocomposites alone and in combination with the miR21/124 without and under magnetic field influence (MF-, MF+) on the morphology, growth pattern and mitochondrial network formation (**A** and **B**) in RAW 264.7. The metabolic activity of RAW 264.7 measured by MTS assay (**C**) and non-significant are marked as ns. The comparisons between groups are marked with brackets. Significant differences are indicated as follows (*p<0,005, **p<0,001 and ***p<0,001) and non-significant are marked as ns. The comparisons between groups are marked with brackets. The black symbols refer to the differences between CTRL and nHAp/IO groups, while red symbols are for nHAp/IO and nHAp/IO@miR-21/124 groups.

The microscopic observation and MTS assay showed that the proliferation activity of RAW 264.7 increase in the presence of nHAp/IO@miR-21/124 biomaterials in MF conditions (Figure 11A–C).

Nevertheless, we have noted a significant decrease in mRNA expression for selected pro-inflammatory markers, including inducible nitric oxide synthase (*iNOS*), tumour necrosis factor-alpha (*TNF-α*) and interleukin 1β (*Il-1β*) (Figure 12A, B and D). Obtained gene expression pattern and decreased ROS accumulation might be associated with alternatively activated macrophages, essential during the wound healing process. This profile can also be reflected by decreased expression of mRNA for (*TGF-β)* noted in

the cultures propagated with nHAp/IO@miR-21/124 without MF presence (Figure 12C).

Bearing in mind that obtained nanometric biomaterials may trigger the expression of pro-osteogenic factors in progenitor cells, we have tested their cytocompatibility under osteogenic conditions. The results showed the mineralization of the extracellular matrix produced by MC3T3-E1. Simultaneously, bone formation under in vitro conditions was promoted not only by MF presence but also by biomaterials' activity (Figure 13). We observed significantly enhanced calcium deposit accumulation, osteogenic nodule formation, and *Coll-1* mRNA expression in MC3T3-E1 cells propagated with nHAp/IO@miR-21/124.
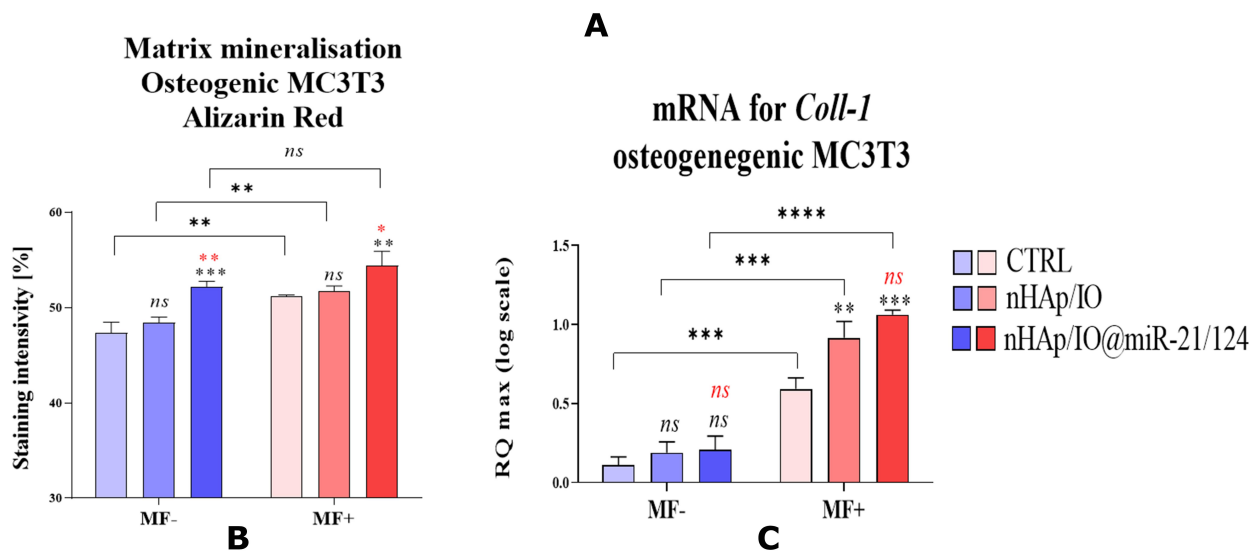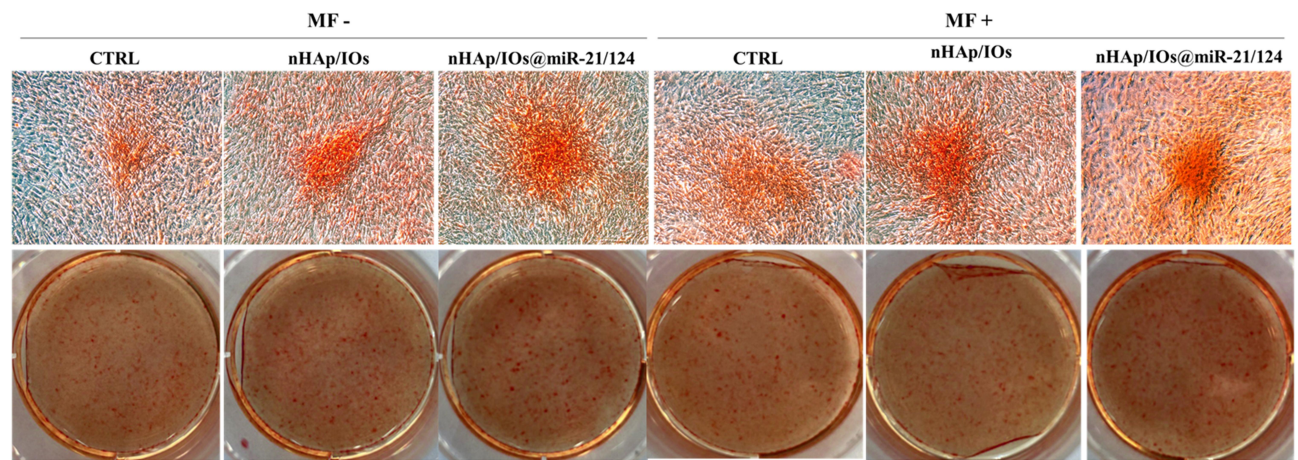
Figure 12 The impact of the nanocomposites alone and in combination with the miR21/124 in the presence of LPS in the condition of MF on the expression of genes associated with inflammatory markers *iNOS* (**A**), *TNFα* (**B**), *TGF-β* (**C**), *IL-1β* (**D**) in RAW 264.7 cell line. Significant differences are indicated as follows (*p<0,005, **p<0,001, ***p<0,001 and ****p<0.0001) and non-significant are marked as ns. The comparisons between groups are marked with brackets. The black symbols refer to the differences between CTRL and nHAp/IO groups, while red symbols are for nHAp/IO and nHAp/IO@miR-21/124 groups.

We have also evaluated the effectiveness of MC3T3-E1 cell line osteogenic differentiation in the presence of the biomaterial, according to the intracellular expression of *Runx-2* and *Opn* on both mRNA and protein expression levels. We have shown that mRNA expression for *Runx-2* and *Opn* decreases during osteogenic differentiation of pre-osteoblast cultured without the magnetic field exposure (Figure 14A–D).

The immunofluorescence of RUNX-2 protein revealed that nHAp/IO@miR-21/124 positively regulates its expression. Moreover, the presence of the magnetic field (MF+) upregulated the RUNX-2 accumulation (Figure 15A and B).

The expression of mRNA coding *Opn* in osteogenic conditions additionally stimulated with MF had the same pattern as samples maintained without MF, ie, indicating that *Opn* mRNA levels were significantly decreased in the presence of biomaterials. The Western blot analysis performed to determine intracellularly accumulated proteins showed that the expression of both RUNX-2 and OPN, increases in response to the biomaterials, but only in the case of MF(-) (Figure 16A–D)

Nevertheless, the immunocytofluorescence staining revealed that nHAp/IO@miR-21/124 support osteogenic differentiation of MC3T3-E1 in both MF conditions. The obtained data showed that the expression of OPN in

Figure 13 The pro-osteogenic impact of the nanocomposites alone and in combination with the miR21/124 evaluated without the magnetic field influence (MF-) and under magnetic field (MF+). The evaluated parameters were matrix mineralization (**A** and **B**) and *Coll-1* (**C**) gene expression in MC3T3-E1 cell line. Significant differences are indicated as follows (*p<0,005, **p<0,001, ***p<0,001 and ****p<0.0001) and non-significant are marked as ns. The comparisons between groups are marked with brackets. The black symbols refer to the differences between CTRL and nHAp/IO groups, while red symbols are for nHAp/IO and nHAp/IO@miR-21/124 groups.

osteogenic cultures of MC3T3-E1 cells was highly promoted by the MF influence and significantly increased in response to functionalised biomaterial nHAp/IO@miR-21/124 (Figure 17A and B).

Discussion

Osteoporosis and difficulties in the healing of osteoporotic bone fractures result from the unbalanced activity of bone-forming (osteoblast) and bone-resorbing (osteoclasts).[9] We have shown previously that magnetic iron particles (IOs) promote the osteogenic activity of progenitor cells.[23] In the current study, nHAp/IO composite was used as a delivery platform for the controlled release of functional microRNAs, ie, miR-21 and miR-124. We have tested the influence of the obtained composite nHAp/IO@miR-21/

124 on viability, morphology, growth pattern, metabolic activity, mitochondrial potential and mitochondrial network development in murine pre-osteoblasts and pre-osteoblasts cell lines. Additionally, the immunomodulatory properties of nHAp/IO@miR-21/124 were evaluated using a monocyte-macrophage cell line – RAW 264.7. We have also tested the effect of the nHAp/IO@miR-21/124 on osteogenesis effectiveness in vitro.

Application of magnetic IO nanoparticles in biomedicine is one of the prospects in various approaches where manipulation by an external magnetic field is required, including hyperthermia treatment, targeted therapies or drug delivery systems.[22,57,58] So far, several attempts have been made to combine hydroxyapatite and IO, especially into the core/shell system to utilise it within
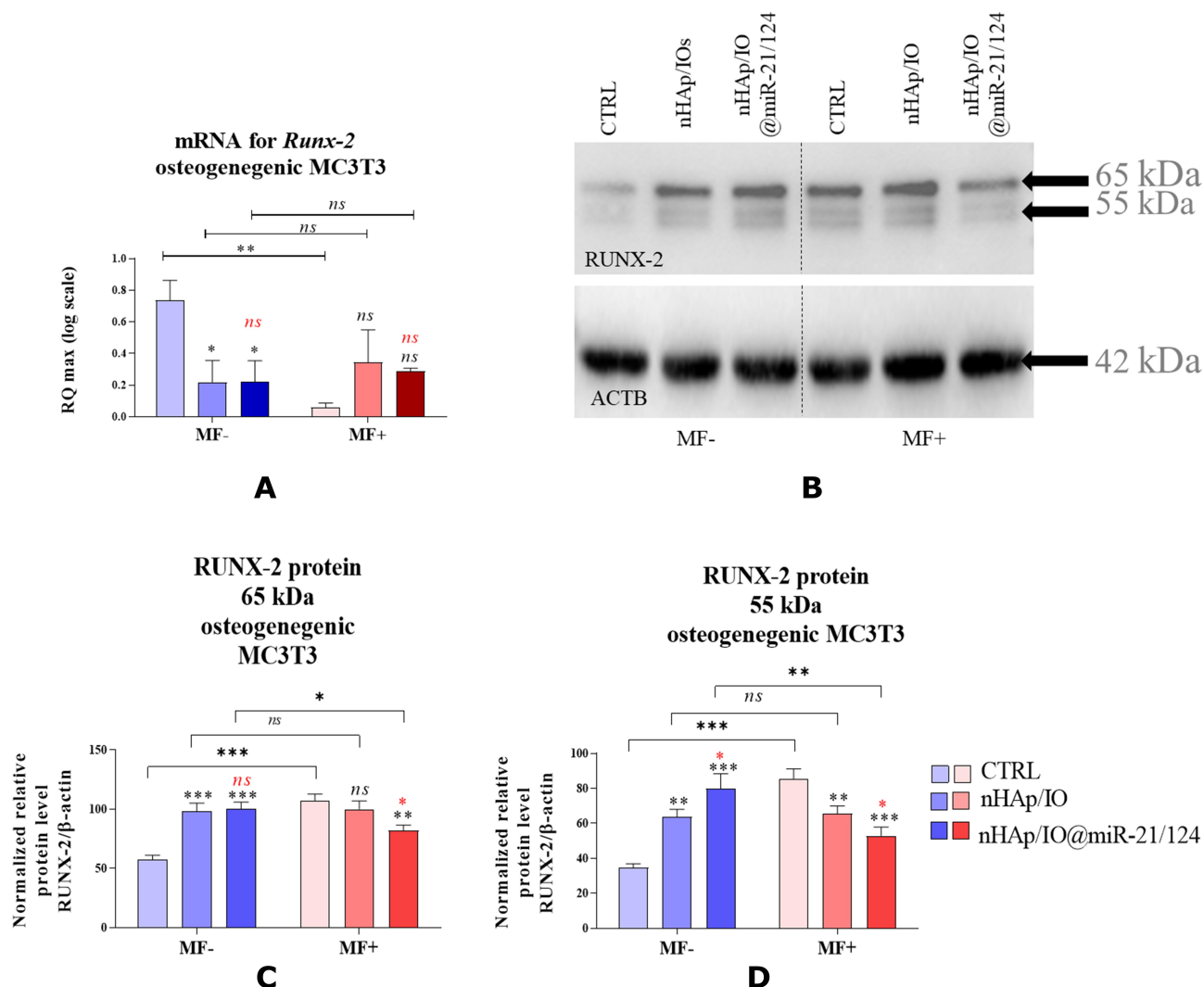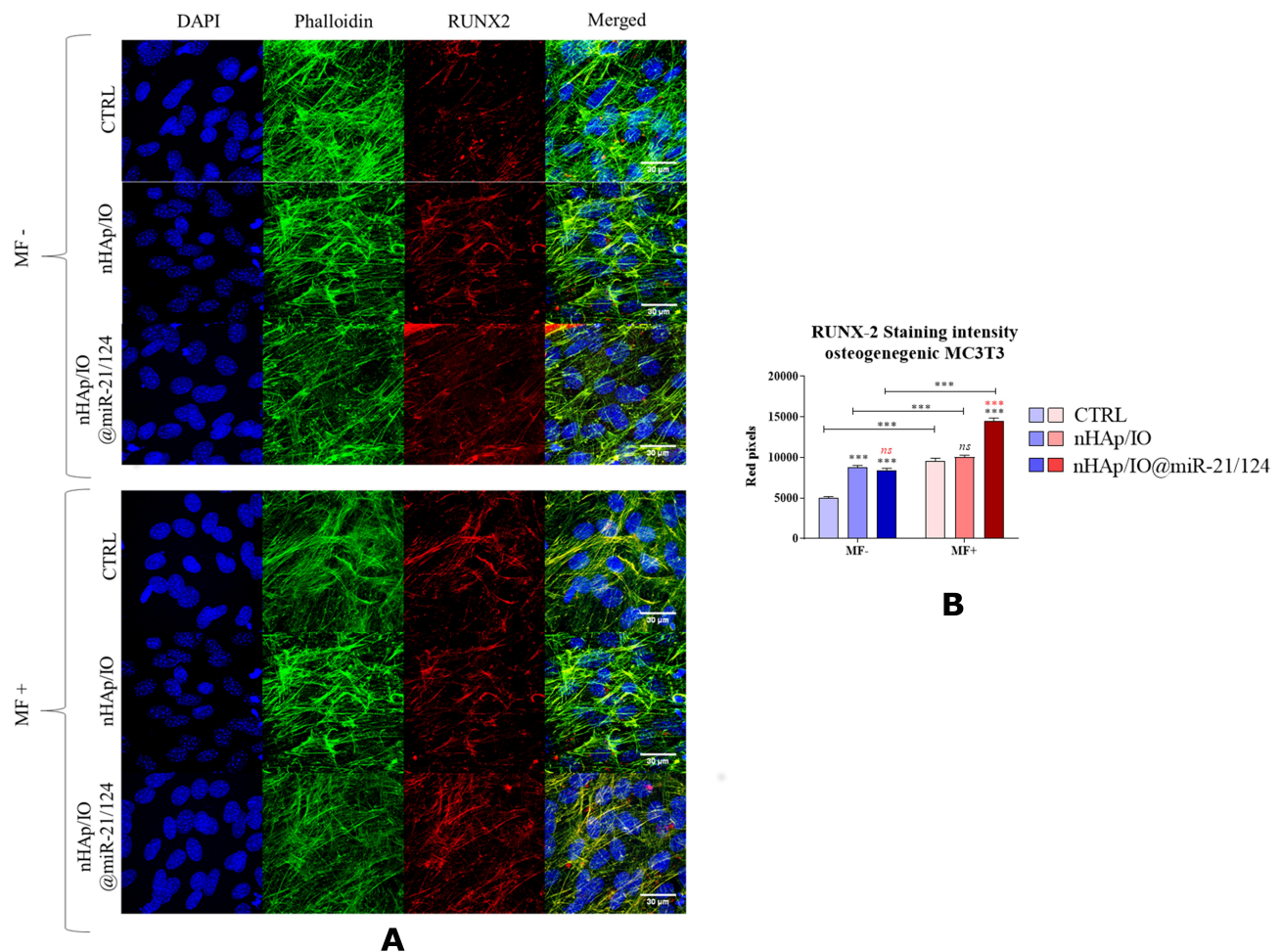
Figure 14 The impact of the nanocomposites alone and in combination with the miR21/124 in the condition of MF on the *Runx-2* gene (**A**) and protein expression level (**B–D**) in MC3T3-E1 cell line Significant differences are indicated as follows (*p<0,005, **p<0,001 and ***p<0,001) and non-significant are marked as ns. The comparisons between groups are marked with brackets. The black symbols refer to the differences between CTRL and nHAp/IO groups, while red symbols are for nHAp/IO and nHAp/IO@miR-21/124 groups.

biomedical fields, eg, tissue engineering and regenerative medicine.[59,60] This work was focused on the nHAp/IO composite, which was successfully obtained by the wet chemistry method. It was found that fabricated nHAp/IO consists of two separate well-crystalised phases (with the content of 68%/32%, respectively) on the nanometric scale with a tendency to mutual agglomeration. Interaction between both phases has been clearly identified using electron microscopy. The IO agglomerates are located close to the nHAp nanoparticles, suggesting surface interaction between them. The magnetic measurements revealed a superparamagnetic character of nHAp/IO at 300 K, while at 2 K the composite showed a ferrimagnetic behaviour. The lower magnetisation values

obtained for the composite compared to the bulk analogue data resulted from the properties of both phases, especially diamagnetic HAp, nanocrystallinity and ability to mutual agglomeration.

In this study, an improvement of pre-osteoblasts viability and metabolic activity was noted in cultures with the nHAp/IO carrying two microRNAs, ie, miR-21 and miR-124. The choice of the miR21 and miR124 as a functional payload was dictated by the previous study revealing their functional role in regulating bone homeostasis.[30,33,61,62] The nHAp/IO@miR-21/124 composite affected osteoblasts and osteoclasts progenitors in a different manner.

The obtained results showed for the first time that the exposition of pre-osteoclasts on nHAp/IO@miR-21/124
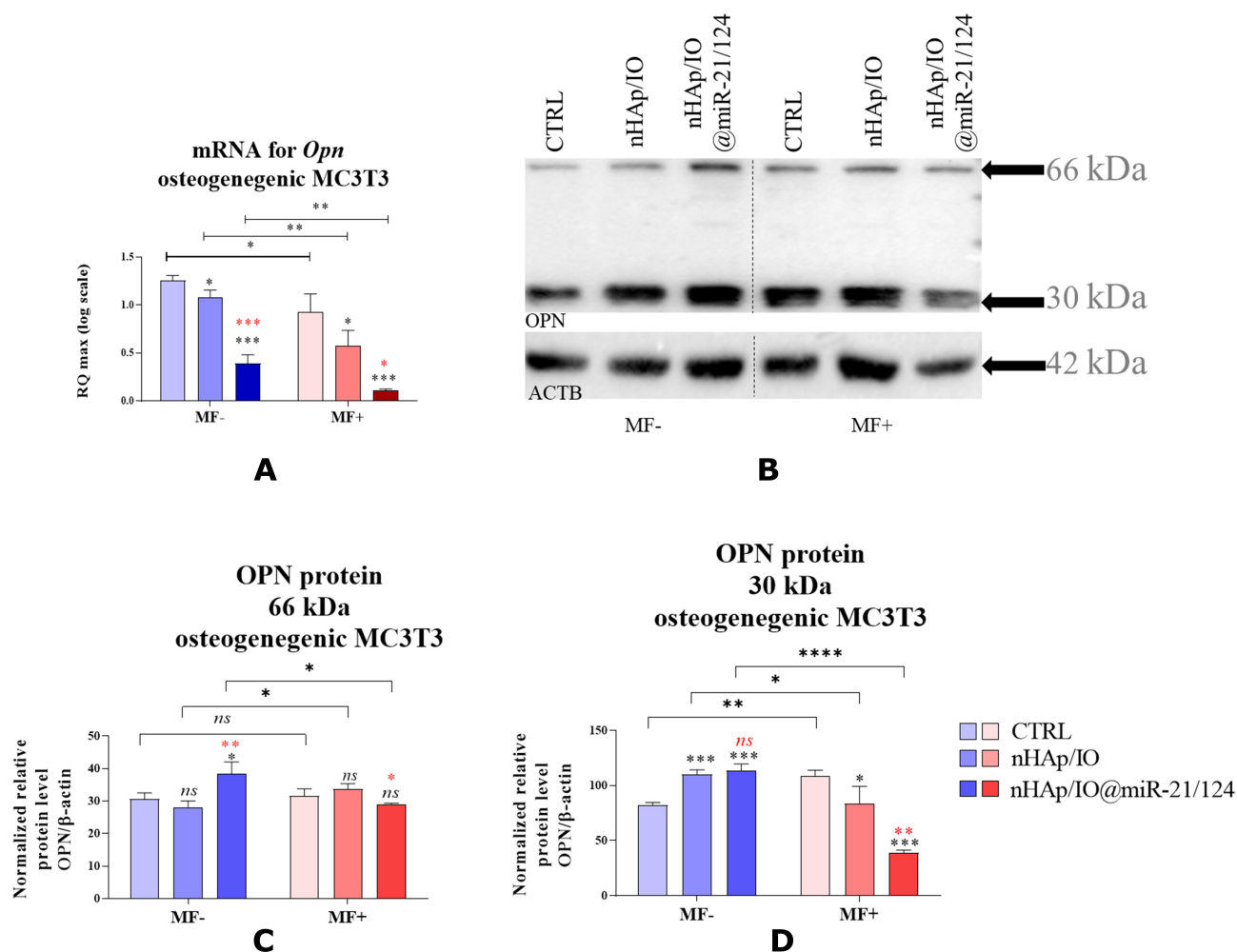
Figure 15 The impact of the nanocomposites alone and in combination with the miR21/124 in the condition of MF on the cytoskeleton morphology and RUNX-2 (**A** and **B**) expression in MC3T3-E1 cell line. Significant differences are indicated (***p<0,001) and non-significant are marked as ns. The comparisons between groups are marked with brackets. The black symbols refer to the differences between CTRL and nHAp/IO groups, while red symbols are for nHAp/IO and nHAp/IO@miR-21/124 groups.

under magnetic field reduces their metabolic activity and decreases expression of markers essential for their functional differentiation. Simultaneously, the nHAp/IO@miR-21/124 composite protects osteoblasts from apoptosis, accompanied by increased mitochondrial metabolism reflected by high mitochondrial membrane potential. Moreover, we have shown that pre-osteoblast cultured with nHAp/IO@miR-21/124 composites were characterized by increased expression of anti-apoptotic *Bcl-2* as well as decreased expression of pro-apoptotic Bax and Bcl-2, while adverse expression pattern was noted in pre-osteoclast cultures. These results stand in good agreement with our previous studies showing the improvement of MF on osteoblasts' viability through the activation of integrin alpha-3.[23] The programmed death of osteoblasts is significant in osteoporotic bone and other bone diseases, including malignant osteolysis.[63] Thus, the anti-apoptotic effect

of nHAp/IO@miR-21/124 toward osteoblast precursors will be essential for bone homeostasis maintenance. The increased osteoblasts survival mediated by nHAp/IO@miR-21/124 was also enhanced under magnetic field exposure, supporting our recent findings.

We have previously noted that MF stimulates the osteogenic potential of human progenitor cells derived from adipose-tissue, activating transcripts essential for osteogenesis regulation, including osteopontin (Opn) osteocalcin (Ocl) and alkaline phosphate (Alp).[64] The magnetic field modulates the multipotency of progenitor cells, promoting their osteogenic differentiation and decreasing adipogenesis.[64,65] In the current study, we confirmed that the osteogenic potential of progenitor cells is stabilized by the magnetic field. Moreover, we indicated on dual action of nHAp/IO@miR-21/124 associated with activation of pro-osteogenic transcripts in osteoblast precursors (MC3T3 cells) and decreased
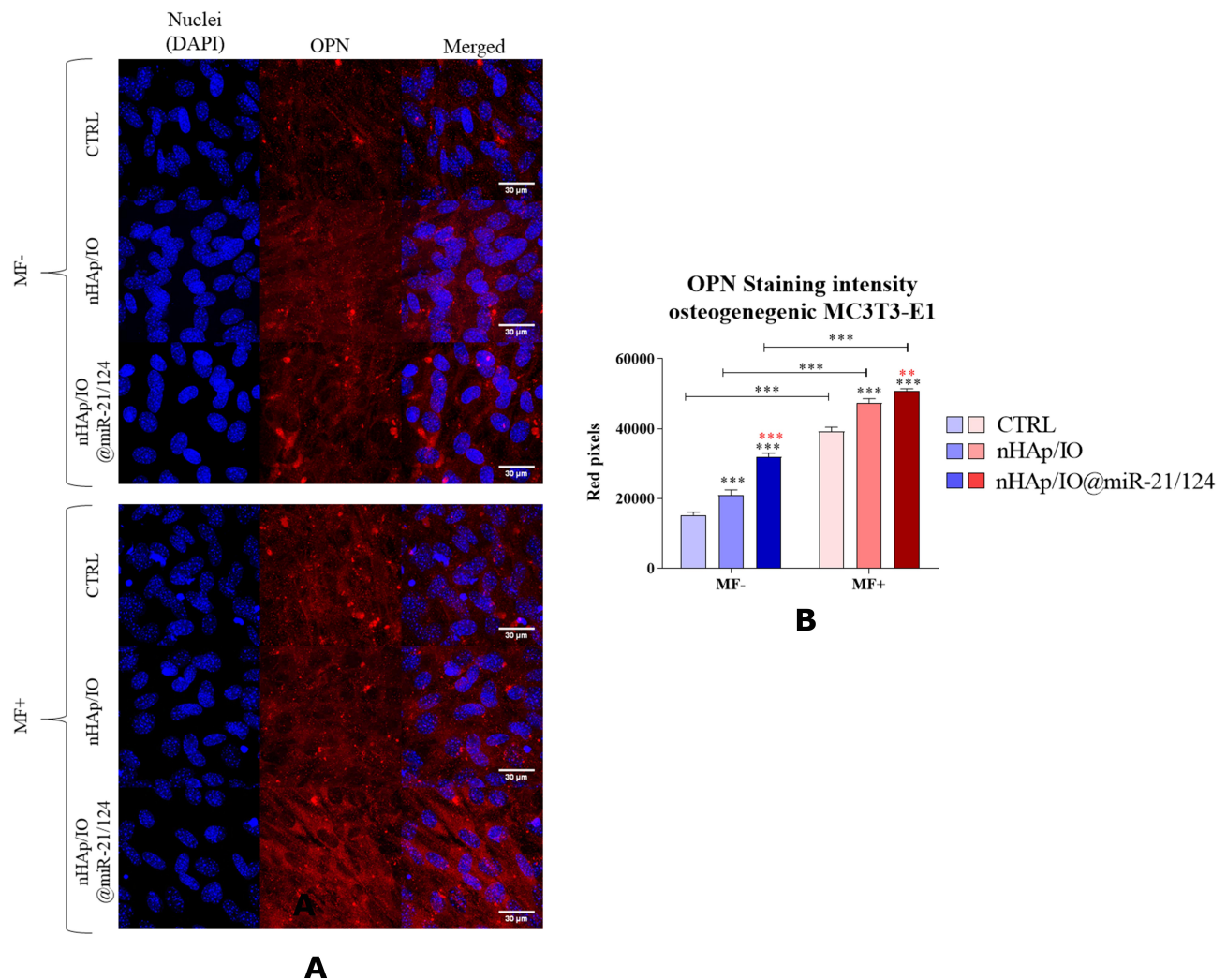
Figure 16 The impact of the nanocomposites alone and in combination with the miR21/124 in condition of MF on the *Opn* gene (**A**) and protein expression level (**B**–**D**) in MC3T3-E1 cell line. Significant differences are indicated as follows (*p<0,005, **p<0,001, ***p<0.001 and ****p<0.0001) and non-significant are marked as ns. The comparisons between groups are marked with brackets. The black symbols refer to the differences between CTRL and nHAp/IO groups, while red symbols are for nHAp/IO and nHAp/IO@miR-21/124 groups.

expression of transcripts critical during osteoclastogenesis in pre-osteoclasts (4B12). The dual effect of the composite triggered by the combination of two antagonistically acting miRNAs will be essential for the regulation of the bone homeostasis process during osteoblasts.

Recently the article published by Wei et al points the role of miR-21 in regulating osteogenic differentiation of stem cells by targeting Smad5 (Smad family member 5), a key regulator of osteogenesis.[61] In turn, Hu et al studies conducted on mice with miR21 knockout showed that miR-21 levels regulate RANKL (receptor activator of nuclear factor κB ligand) and OPG expression targeting Sprouty 1 (Spry1). It was also proved that miR-21 played a role in protecting bone degeneration and inhibition of bone resorption through PDCD4 (programmed cell death 4).[28] Moreover, the inhibition of the miR-21

in osteoblasts results in impairment of differentiation and extracellular matrix (ECM) mineralization.[33] More importantly, decreased miR-21 levels disrupt the paracrine signalling, leading to a decrease in the viability of pre-osteoclasts. The osteoprotective effect of miR-21 relies on the pro-survival effect toward osteoblasts and regulation of their interplay with osteoclasts.[33] Moreover, the inhibition of the osteoclasts metabolic activity and their viability observed in this study might be directly regulated by miR-124.[30,66] Tang et al proved that miR-124 attenuates osteoclastogenic differentiation of bone marrow-derived monocytes through interaction with Rab27a.[30] Moreover, it was shown that miR-124 act as a negative regulator of osteogenic differentiation and bone development in vivo and its mechanism of action includes targeting Dlx5, Dlx3 and Dlx2 genes.[62]

Figure 17 The impact of the nanocomposites alone and in combination with the miR21/124 in condition of MF on the OPN expression (**A** and **B**) in MC3T3-E1 cell line. Significant differences are indicated as follows (**p<0,001 and ***p<0,001) and non-significant are marked as ns. The comparisons between groups are marked with brackets. The black symbols refer to the differences between CTRL and nHAp/IO groups, while red symbols are for nHAp/IO and nHAp/IO@miR-21/124 groups.

The obtained results confirmed that the new proposed biomaterial, ie, nHAp/IO@miR-21/124, exhibits an immunomodulatory effect towards monocyte-macrophage cell line RAW 264.7 with LPS-induced inflammatory phenotype. The immunomodulatory action of the composite was also regulated by exposure to the magnetic field.

Typically, macrophages are known for their remarkable plasticity response to various stimuli and undergo multidirectional changes after stimulation.[67] Macrophage exposure to the bacterial derived LPS initiates complex signal transduction leading to the secretion of the proinflammatory cytokine profiles, enhanced anti-cancer and anti-bacterial activity.[68] In addition, LPS as an immodulatory compound is used for priming phagocytes and mediates enhanced ROS secretion.[69,70] In this study, we have shown

that nHAp/IO@miR-21/124 decreases the intracellular accumulation of ROS by RAW 264.7 cells stimulated by LPS, both under MF influence and without.

The anti-inflammatory action of the static magnetic field and hydroxyapatites were described previously.[35,71] Here we showed that the anti-inflammatory potential of nHAp/IO composites could be enhanced by incorporating miR-21 and miR-124 molecules. The improved biological effects resulting from nHAp/IO functionalization by miRNAs was evidenced by the proinflammatory profiles of cytokines released by LPS-stimulated macrophages in experimental cultures. Our actual results showed decreased expression of TNF-α and IL-1β, the master regulators of the inflammation in osteoporotic bones. Moreover, macrophages exposed to the nHAp/IO@miR-
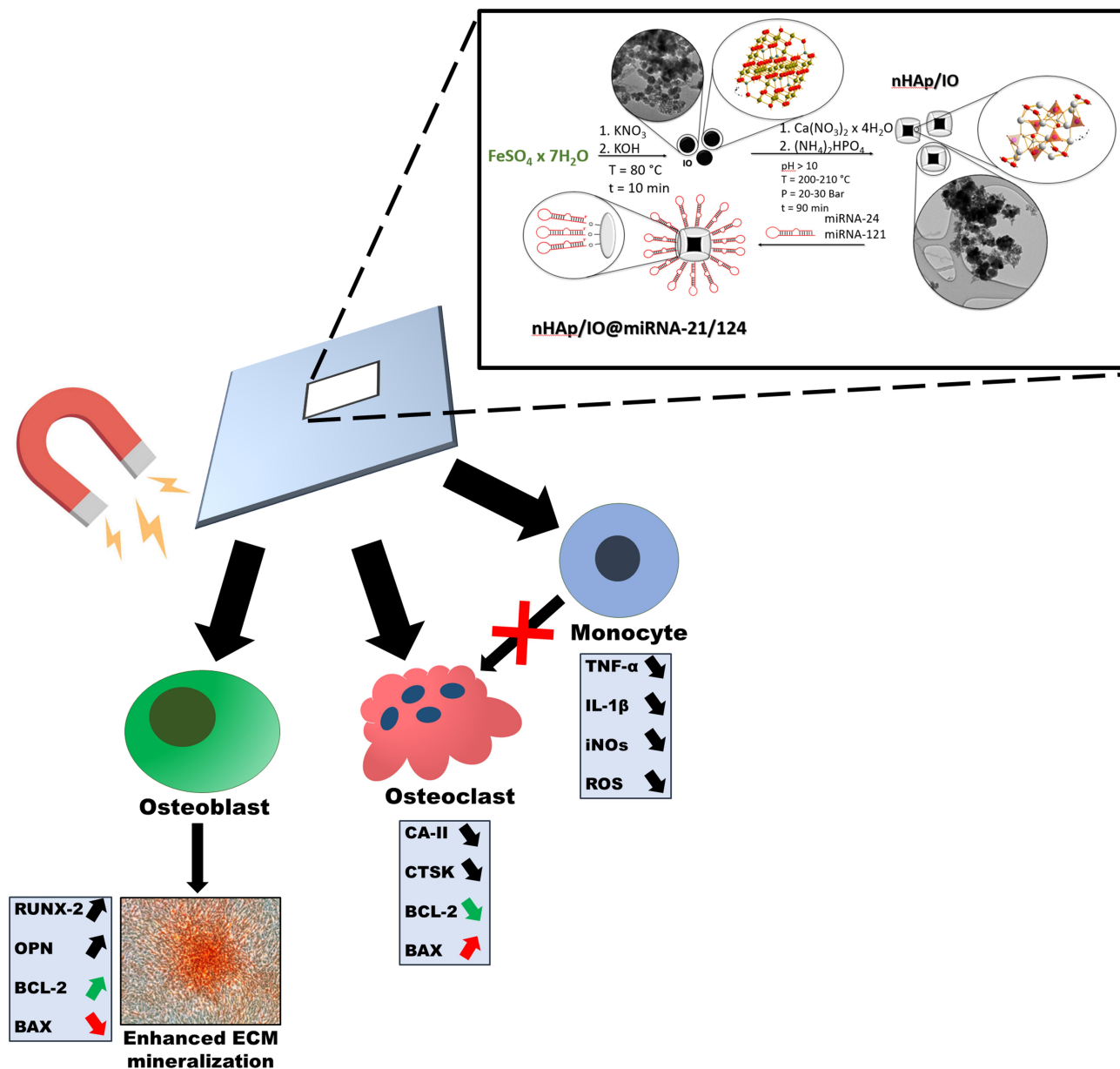
Figure 18 The graphical summary of the study.

21/124 showed decreased expression of inducible nitric oxide synthase (iNOS), a significant mediator of inflammation that contributes to cell apoptosis. This molecule mediates the balance between M1 and M2 macrophages polarization by modifying IRF5 (member of interferon regulatory factor).[67,72] Thus, iNOS is a hallmark molecule of M1 classical pathway-activated macrophages involved in the pathogenesis of inflammatory diseases.[73] Furthermore, pathological conditions associated with inflammation provide molecular and cellular signals essential for osteoclast differentiation from the monocytes precursors.[72] Thus, the decreased expression of transcripts

essential during osteoclastogenesis, namely carbonic anhydrase II and cathepsin K, noted in cultures with nHAp/IO@miR-21/124 may also be associated with its immunomodulatory effect.

The pro-survival effect of nHAp/IO@miR-21/124 toward osteoblast progenitors and its anti-inflammatory potential will be beneficial in terms of osteoporotic bone healing and proper bone remodelling. Thus, we also tested the influence of nHAp/IO@miR-21/124 composites on osteogenic differentiation of osteoblast precursors, ie, MC3T3-E1 cells, monitoring functional mineralization of extracellular matrix (ECM) and expression of RUNX-2

and osteopontin (OPN) expression. The deficiency or mutations of RUNX-2 may cause abnormalities in bone homeostasis.[74] While osteopontin, together with osteocalcin, are key players in both the biological and mechanical function of bones.[75] Generally, these two non-collagenous proteins (NCPs) are integral components of extracellular matrix (ECM), secreted during the formation of bone, mainly in the process of mineralization due to their regulations modes in directly and indirectly controlling of mass, mineral size and bone orientation.[75,76] Furthermore, we showed that RUNX-2 and OPN are regulated by miR-21 levels influencing osteoblast and osteoclast coupling. This study showed that nHAp/IO@miR-21/124 modulates the expression of both RUNX-2 and OPN, promoting the formation of a functional mineralized matrix. The molecular levels of RUNX-2 and OPN were affected by the exposure to the magnetic field, which also reflects the dynamics of osteogenesis in vitro. Collectively, the obtained data indicating the modulatory effect of nHAp/IO@miR-21/124 on osteoblast and osteoclast activity shed a favourable light for future application of this novel composite as a platform for guided regeneration of osteoporotic bone in situ (Figure 18).

Conclusion

Osteoporosis is a complex metabolic disease of bone affecting 200 million people worldwide. Moreover, in terms of senile osteoporosis associated with a progressive decline of an organism's regenerative potential, innovative methods of treatment, combining the approaches of tissue engineering triad are highly required. The homeostasis of bone tissue in the course of osteoporosis is disturbed due to imbalanced coupling between bone-forming and bone-resorbing cells. The regeneration of osteoporotic bone is challenging but can be supported by intelligent biomaterials promoting the regeneration of bone in situ. In this study, we have developed a novel composite nHAp/IO@miR21/124 that possess the properties of an intelligent biomaterial for guided regeneration of osteoporotic bone. The nHAp/IO@miR21/124 improves metabolism of pre-osteoblasts and promotes osteogenesis, simultaneously decreasing differentiation of pre-osteoclasts. This biological effect was obtained due to the application of nHap/IO composite as a delivery platform for therapeutic miRNAs acting antagonistically and released under magnetic field. The proposed system may improve bone metabolism by promoting pro-osteogenic signalling pathways and regulating the balance between bone-forming and bone-resorbing cells.

Abbreviations

nHAp, nanohydroxyapatite; IOs, iron oxide nanoparticles; miR, microRNA; RT-qPCR, quantitative polymerase chain reaction followed by reverse transcription; XRPD, X-ray powder diffraction; FT-IR, Fourier-transform infrared spectroscopy; SEM-EDS, scanning electron microscopy with energy dispersive spectroscopy; HRTEM, high-resolution transmission electron microscopy; SAED, selected area diffraction; LPS, lipopolysaccharide; MF, magnetic field; Runx-2, runt-related transcription factor 2; Coll-1, collagen type 1; *TNF-α*, tumour necrosis factor *α; TGF-β*, transforming growth factor *β; IL-1β*, interleukin type *1β; BMI*, body mass index; *T1D*, type 1 diabetes; *T2D*, type 2 diabetes; NIH, National Institutes of Health; SERMs, selective estrogen receptor modulators; PTH, parathormone; RANKL, receptor activator for nuclear factor κ β ligand; RANK, receptor activator for nuclear factor κ β; OPG, osteoprotegerin; LGR4, leucine rich repeat containing G protein-coupled receptor 4; Ephrin2/ephB4, ephrin 2/EPH receptor B4 pathway; Fas/FasL, fas cell surface death receptor/Fas ligand pathway; Bcl-2, B-cell lymphoma 2; BAX, Bcl-2 associated X protein; P21, cyclin-dependent kinase inhibitor 1; P53, tumour protein P53; INT-a3, integrin a3; TRAP, tartrate-resistant acid phosphatase; OPN, osteopontin; BMP2, bone morphogenetic protein type 2; ALP, alkaline phosphatase; MRI, magnetic resonance imaging; BM-MSCs, bone marrow mesenchymal stem cells; Spry1, protein sprouty homolog 1; Spry2, protein sprouty homolog 2; PDCD4, programmed cell death 4; NFATc1, nuclear factor of activated T cells 1; Bad, Bcl-2 associated agonist of cell death; Mmp-9, metalloproteinase 9; CAII, carbonic anhydrase II; Ctsk, cathepsin K; Gapdh, glyceraldehyde 3-phosphate dehydrogenase; iNOS, nitric oxide synthase; MCL-1, myeloid cell leukemia 1; Bak, Bcl-2 homologous antagonist killer; Bim, Bcl-2 like 11; Bid, BH3 interacting-domain death agonist; Puma, p53 upregulated modulator of apoptosis; Noxa, phorbol-12-myristate-13-acetate-induced protein 1; OCN, osteonectin; ECM, extracellular matrix; Dlx5, distal-less homeobox 5 protein; Dlx3, distal-less homeobox 3 protein; Dlx2, distal-less homeobox 2 protein; NCPs, noncollagenous proteins.

No. UMO 2017/26/M/NZ5/01184)" The publication is financed under the Leading Research Groups support project from the subsidy increased for the period 2020–2025 in the amount of 2% of the subsidy referred to Art. 387 (3) of the Law of 20 July 2018 on Higher Education and Science, obtained in 2019.

Disclosure

The authors report no conflicts of interest in this work.

References

1. Porter JL, Varacallo M. Osteoporosis. StatPearls. StatPearls Publishing; 2021. Available from: http://www.ncbi.nlm.nih.gov/books/NBK441901/. Accessed March 23, 2021.
2. Johnston CB, Dagar M. Osteoporosis in older adults. *Med Clin North Am*. 2020;104(5):873–884. doi:10.1016/j.mcna.2020.06.004
3. Bijelic R, Milicevic S, Balaban J. Risk factors for osteoporosis in postmenopausal women. *Med Arch*. 2017;71(1):25–28. doi:10.5455/medarh.2017.71.25-28
4. Huang J-F, Wu Q-N, Zheng X-Q, et al. The characteristics and mortality of osteoporosis, osteomyelitis, or rheumatoid arthritis in the diabetes population: a Retrospective Study. *Int J Endocrinol*. 2020;2020:8821978. doi:10.1155/2020/8821978
5. Hernlund E, Svedbom A, Ivergård M, et al. Osteoporosis in the European Union: medical management, epidemiology and economic burden. A report prepared in collaboration with the International Osteoporosis Foundation (IOF) and the European Federation of Pharmaceutical Industry Associations (EFPIA). *Arch Osteoporos*. 2013;8:136. doi:10.1007/s11657-013-0136-1
6. Stanghelle B, Bentzen H, Giangregorio L, Pripp AH, Bergland A. Associations between health-related quality of life, physical function and pain in older women with osteoporosis and vertebral fracture. *BMC Geriatr*. 2019;19(1):298. doi:10.1186/s12877-019-1268-y
7. Ukon Y, Makino T, Kodama J, et al. Molecular-based treatment strategies for osteoporosis: a literature review. *Int J Mol Sci*. 2019;20(10). doi:10.3390/ijms20102557
8. Hsieh C-Y, Sung S-F, Huang H-K. Drug treatment strategies for osteoporosis in stroke patients. *Expert Opin Pharmacother*. 2020;21(7):811–821. doi:10.1080/14656566.2020.1736556
9. Ensrud KE, Crandall CJ. Osteoporosis. *Ann Intern Med*. 2017;167(3):ITC17–ITC32. doi:10.7326/AITC201708010
10. Ballane G, Cauley JA, Luckey MM, El-Hajj Fuleihan G. Worldwide prevalence and incidence of osteoporotic vertebral fractures. *Osteoporos Int*. 2017;28(5):1531–1542. doi:10.1007/s00198-017-3909-3
11. Zeytinoglu M, Jain RK, Vokes TJ. Vertebral fracture assessment: enhancing the diagnosis, prevention, and treatment of osteoporosis. *Bone*. 2017;104:54–65. doi:10.1016/j.bone.2017.03.004
12. Chen X, Wang Z, Duan N, Zhu G, Schwarz EM, Xie C. Osteoblast-osteoclast interactions. *Connect Tissue Res*. 2018;59(2):99–107. doi:10.1080/03008207.2017.1290085
13. Kenkre JS, Bassett J. The bone remodelling cycle. *Ann Clin Biochem*. 2018;55(3):308–327. doi:10.1177/0004563218759371
14. Infante A, Rodríguez CI. Osteogenesis and aging: lessons from mesenchymal stem cells. *Stem Cell Res Ther*. 2018;9(1):244. doi:10.1186/s13287-018-0995-x
15. Gaffney-Stomberg E. The impact of trace minerals on bone metabolism. *Biol Trace Elem Res*. 2019;188(1):26–34. doi:10.1007/s12011-018-1583-8
16. Sathiyavimal S, Vasantharaj S, LewisOscar F, Selvaraj R, Brindhadevi K, Pugazhendhi A. Natural organic and inorganic–hydroxyapatite biopolymer composite for biomedical applications. *Prog Org Coat*. 2020;147:105858. doi:10.1016/j.porgcoat.2020.105858
17. Qayoom I, Teotia AK, Kumar A. Nanohydroxyapatite based ceramic carrier promotes bone formation in a femoral neck canal defect in osteoporotic rats. *Biomacromolecules*. 2020;21(2):328–337. doi:10.1021/acs.biomac.9b01327
18. Sathiyavimal S, Vasantharaj S, LewisOscar F, Pugazhendhi A, Subashkumar R. Biosynthesis and characterization of hydroxyapatite and its composite (hydroxyapatite-gelatin-chitosan-fibrin-bone ash) for bone tissue engineering applications. *Int J Biol Macromol*. 2019;129:844–852. doi:10.1016/j.ijbiomac.2019.02.058
19. Varadavenkatesan T, Vinayagam R, Pai S, Kathirvel B, Pugazhendhi A, Selvaraj R. Synthesis, biological and environmental applications of hydroxyapatite and its composites with organic and inorganic coatings. *Prog Org Coat*. 2021;151:106056. doi:10.1016/j.porgcoat.2020.106056
20. Smieszek A, Marycz K, Szustakiewicz K, et al. New approach to modification of poly (l-lactic acid) with nano-hydroxyapatite improving functionality of human adipose-derived stromal cells (hASCs) through increased viability and enhanced mitochondrial activity. *Mater Sci Eng C Mater Biol Appl*. 2019;98:213–226. doi:10.1016/j.msec.2018.12.099
21. Kim J-M, Lin C, Stavre Z, Greenblatt MB, Shim J-H. Osteoblast-osteoclast communication and bone homeostasis. *Cells*. 2020;9(9). doi:10.3390/cells9092073
22. Vasantharaj S, Sathiyavimal S, Senthilkumar P, LewisOscar F, Pugazhendhi A. Biosynthesis of iron oxide nanoparticles using leaf extract of Ruellia tuberosa: antimicrobial properties and their applications in photocatalytic degradation. *J Photochem Photobiol B*. 2019;192:74–82. doi:10.1016/j.jphotobiol.2018.12.025
23. Marycz K, Sobierajska P, Roecken M, et al. Iron oxides nanoparticles (IOs) exposed to magnetic field promote expression of osteogenic markers in osteoblasts through integrin alpha-3 (INTa-3) activation, inhibits osteoclasts activity and exerts anti-inflammatory action. *J Nanobiotechnology*. 2020:18. doi:10.1186/s12951-020-00590-w.
24. Chaudhary V, Jangra S, Yadav NR. Nanotechnology based approaches for detection and delivery of microRNA in healthcare and crop protection. *J Nanobiotechnology*. 2018;16(1):40. doi:10.1186/s12951-018-0368-8
25. Tzameret A, Ketter-Katz H, Edelshtain V, et al. In vivo MRI assessment of bioactive magnetic iron oxide/human serum albumin nanoparticle delivery into the posterior segment of the eye in a rat model of retinal degeneration. *J Nanobiotechnol*. 2019;17(1):3. doi:10.1186/s12951-018-0438-y
26. Sikora M, Marycz K, Smieszek A. Small and long non-coding RNAs as functional regulators of bone homeostasis, acting alone or cooperatively. *Mol Ther Nucleic Acids*. 2020;21:792–803. doi:10.1016/j.omtn.2020.07.017
27. Wu D, Kang L, Tian J, et al. Exosomes derived from bone mesenchymal stem cells with the stimulation of Fe_3O_4 nanoparticles and static magnetic field enhance wound healing through upregulated miR-21-5p. *IJN*. 2020;15:7979–7993. doi:10.2147/IJN.S275650
28. Hu C-H, Sui B-D, Du F-Y, et al. miR-21 deficiency inhibits osteoclast function and prevents bone loss in mice. *Sci Rep*. 2017;7(1):43191. doi:10.1038/srep43191
29. Lee Y, Kim HJ, Park CK, et al. MicroRNA-124 regulates osteoclast differentiation. *Bone*. 2013;56(2):383–389. doi:10.1016/j.bone.2013.07.007

30. Tang L, Yin Y, Liu J, Li Z, Lu X. MiR-124 attenuates osteoclastogenic differentiation of bone marrow monocytes via targeting Rab27a. *Cell Physiol Biochem*. 2017;43(4):1663–1672. doi:10.1159/000484027

31. McCusker LB, Von Dreele RB, Cox DE, Louër D, Scardi P. Rietveld refinement guidelines. *J Appl Cryst*. 1999;32(1):36–50. doi:10.1107/S0021889898009856

32. Amano S, Sekine K, Bonewald L, Ohmori Y. A novel osteoclast precursor cell line, 4b12, recapitulates the features of primary osteoclast differentiation and function: enhanced transfection efficiency before and after differentiation. *J Cell Physiol*. 2009;221(1):40–53. doi:10.1002/jcp.21827

33. Smieszek A, Marcinkowska K, Pielok A, Sikora M, Valihrach L, Marycz K. The Role of miR-21 in osteoblasts-osteoclasts coupling in vitro. *Cells*. 2020;9:2. doi:10.3390/cells9020479

34. Marycz K, Alicka M, Kornicka-Garbowska K, et al. Promotion through external magnetic field of osteogenic differentiation potential in adipose-derived mesenchymal stem cells: design of polyurethane/poly (lactic) acid sponges doped with iron oxide nanoparticles. *J Biomed Mater Res B Appl Biomater*. 2020;108(4):1398–1411. doi:10.1002/jbm.b.34488

35. Sikora M, Marcinkowska K, Marycz K, Wiglusz RJ, Śmieszek A. The Potential Selective Cytotoxicity of Poly (L- Lactic Acid)-Based Scaffolds Functionalized with Nanohydroxyapatite and Europium (III) Ions toward Osteosarcoma Cells. *Materials*. 2019;12(22):3779. doi:10.3390/ma12223779

36. Targonska S, Sikora M, Marycz K, Smieszek A, Wiglusz RJ. Theranostic applications of nanostructured silicate-substituted hydroxyapatite codoped with eu3+ and bi3+ ions-a novel strategy for bone regeneration. *ACS Biomater Sci Eng*. 2020;6(11):6148–6160. doi:10.1021/acsbiomaterials.0c00824

37. Alicka M, Kornicka-Garbowska K, Kucharczyk K, Kępska M, Röcken M, Marycz K. Age-dependent impairment of adipose-derived stem cells isolated from horses. *Stem Cell Res Ther*. 2020;11(1):4. doi:10.1186/s13287-019-1512-6

38. Smieszek A, Tomaszewski KA, Kornicka K, Marycz K. Metformin promotes osteogenic differentiation of adipose-derived stromal cells and exerts pro-osteogenic effect stimulating bone regeneration. *J Clin Med*. 2018;7(12). doi:10.3390/jcm7120482

39. Smieszek A, Seweryn A, Marcinkowska K, et al. Titanium dioxide thin films obtained by atomic layer deposition promotes osteoblasts' viability and differentiation potential while inhibiting osteoclast activity-potential application for osteoporotic bone regeneration. *Materials (Basel)*. 2020;13(21). doi:10.3390/ma13214817

40. Elayaraja K, Rajesh P, Ahymah Joshy MI, et al. Enhancement of wettability and antibiotic loading/release of hydroxyapatite thin film modified by 100MeV Ag7+ ion irradiation. *Mater Chem Phys*. 2012;134(1):464–477. doi:10.1016/j.matchemphys.2012.03.018

41. Yamanaka T, Shimazu H, Ota K. Electric conductivity of Fe2SiO4–Fe3O4 spinel solid solutions. *Phys Chem Min*. 2001;28(2):110–118. doi:10.1007/s002690000137

42. Gawande MB, Branco PS, Varma RS. Nano-magnetite (Fe3O4) as a support for recyclable catalysts in the development of sustainable methodologies. *Chem Soc Rev*. 2013;42(8):3371–3393. doi:10.1039/C3CS35480F

43. Zawisza K, Sobierajska P, Nowak N, et al. Preparation and preliminary evaluation of bio-nanocomposites based on hydroxyapatites with antibacterial properties against anaerobic bacteria. *Mater Sci Eng C*. 2020;106:110295. doi:10.1016/j.msec.2019.110295

44. Foroughi F, Hassanzadeh-Tabrizi SA, Bigham A. In situ microemulsion synthesis of hydroxyapatite-MgFe2O4 nanocomposite as a magnetic drug delivery system. *Mater Sci Eng C*. 2016;68:774–779. doi:10.1016/j.msec.2016.07.028

45. Sangeetha K, Ashok M, Girija EK. Development of multifunctional cobalt ferrite/hydroxyapatite nanocomposites by microwave assisted wet precipitation method: a promising platform for synergistic chemo-hyperthermia therapy. *Ceram Int*. 2019;45(10):12860–12869. doi:10.1016/j.ceramint.2019.03.209

46. Sobierajska P, Wiglusz RJ. Influence of Li+ ions on the physicochemical properties of nanocrystalline calcium–strontium hydroxyapatite doped with Eu3+ ions. *New J Chem*. 2019;43 (37):14908–14916. doi:10.1039/C9NJ03003D

47. Szyszka K, Rewak-Soroczynska J, Dorotkiewicz-Jach A, et al. Structural modification of nanohydroxyapatite Ca10(PO4)6(OH)2 related to Eu3+ and Sr2+ ions doping and its spectroscopic and antimicrobial properties. *J Inorg Biochem*. 2020;203:110884. doi:10.1016/j.jinorgbio.2019.110884

48. Ansari A, Vahedi S, Tavakoli O, Khoobi M, Faramarzi MA. Novel Fe 3 O 4/hydroxyapatite/β-cyclodextrin nanocomposite adsorbent: synthesis and application in heavy metal removal from aqueous solution. *Appl Organomet Chem*. 2019;33(1):e4634. doi:10.1002/aoc.4634

49. Bang LT, Long BD, Othman R. Carbonate hydroxyapatite and silicon-substituted carbonate hydroxyapatite: synthesis, mechanical properties, and solubility evaluations. *Scientific World J*. 2014;2014:1–9. doi:10.1155/2014/969876

50. Yao S, Yan X, Zhao Y, Li B, Sun L. Selective binding and magnetic separation of histidine-tagged proteins using Ni2+-decorated Fe3O4/hydroxyapatite composite nanoparticles. *Mater Lett*. 2014;126:97–100. doi:10.1016/j.matlet.2014.04.022

51. Wei Y, Han B, Hu X, Lin Y, Wang X, Deng X. Synthesis of Fe3O4 nanoparticles and their magnetic properties. *Procedia Eng*. 2012;27:632–637. doi:10.1016/j.proeng.2011.12.498

52. Bhowmik RN, Ranganathan R, Nagarajan R, Ghosh B, Kumar S. Role of strain-induced anisotropy on magnetic enhancement in mechanically alloyed Co 0.2 Zn 0.8 Fe 2 O 4 nanoparticle. *Phys Rev B*. 2005;72(9):094405. doi:10.1103/PhysRevB.72.094405

53. Ghosh B, Kumar S, Poddar A, et al. Spin glasslike behavior and magnetic enhancement in nanosized Ni–Zn ferrite system. *J Appl Phys*. 2010;108(3):034307. doi:10.1063/1.3456174

54. Saravanan P, Alam S, Mathur GN. Comparative study on the synthesis of γ-Fe2O3 and Fe3O4 nanocrystals using high-temperature solution-phase technique. *J Mater Sci Lett*. 2003;22(18):1283–1285. doi:10.1023/A:1025470405000

55. Woo K, Hong J, Choi S, et al. Easy synthesis and magnetic properties of iron oxide nanoparticles. *Chem Mater*. 2004:16. doi:10.1021/cm049552x.

56. Singh AK, Srivastava ON, Singh K. Shape and size-dependent magnetic properties of fe3o4 nanoparticles synthesized using piperidine. *Nanoscale Res Lett*. 2017;12(1):298. doi:10.1186/s11671-017-2039-3

57. Glenske K, Donkiewicz P, Köwitsch A, et al. Applications of metals for bone regeneration. *Int J Mol Sci*. 2018;19(3):826. doi:10.3390/ijms19030826

58. Amiri M, Salavati-Niasari M, Akbari A. Magnetic nanocarriers: evolution of spinel ferrites for medical applications. *Adv Colloid Interface Sci*. 2019;265:29–44. doi:10.1016/j.cis.2019.01.003

59. Tkachenko MV, Kamzin AS. Synthesis and properties of hybrid hydroxyapatite–ferrite (Fe3O4) particles for hyperthermia applications. *Phys Solid State*. 2016;58(4):763–770. doi:10.1134/S1063783416040260

60. Vlasova M, Fedotov A, Mendoza Torres I, Kakazey M, Komlev V, Marquez Aguilar PA. Mechanosynthesis of hydroxyapatite–ferrite composite nanopowder. *Ceram Int*. 2017;43(8):6221–6231. doi:10.1016/j.ceramint.2017.02.020

61. Wei F, Yang S, Guo Q, et al. MicroRNA-21 regulates osteogenic differentiation of periodontal ligament stem cells by targeting smad5. *Sci Rep*. 2017;7(1):16608. doi:10.1038/s41598-017-16720-8

62. Qadir AS, Um S, Lee H, et al. miR-124 negatively regulates osteogenic differentiation and in vivo bone formation of mesenchymal stem cells. *J Cell Biochem*. 2015;116(5):730–742. doi:10.1002/jcb.25026

63. Mollazadeh S, Fazly Bazzaz BS, Kerachian MA. Role of apoptosis in pathogenesis and treatment of bone-related diseases. *J Orthop Surg Res*. 2015;10. doi:10.1186/s13018-015-0152-5

64. Marędziak M, Śmieszek A, Tomaszewski KA, Lewandowski D, Marycz K. The effect of low static magnetic field on osteogenic and adipogenic differentiation potential of human adipose stromal/stem cells. *J Magn Magn Mater*. 2016;398:235–245. doi:10.1016/j.jmmm.2015.09.004

65. Marędziak M, Tomaszewski K, Polinceusz P, Lewandowski D, Marycz K. Static magnetic field enhances the viability and proliferation rate of adipose tissue-derived mesenchymal stem cells potentially through activation of the phosphoinositide 3-kinase/Akt (PI3K/Akt) pathway. *Electromagn Biol Med*. 2017;36(1):45–54. doi:10.3109/15368378.2016.1149860

66. Tang S-L, Huang Q-H, Wu L-G, Liu C, Cai A-L. MiR-124 regulates osteoblast differentiation through GSK-3β in ankylosing spondylitis. *Eur Rev Med Pharmacol Sci*. 2018;22(20):6616–6624. doi:10.26355/eurrev_201810_16136

67. Horwood NJ. Macrophage polarization and bone formation: a review. *Clinic Rev Allerg Immunol*. 2016;51(1):79–86. doi:10.1007/s12016-015-8519-2

68. Ciesielska A, Matyjek M, Kwiatkowska K. TLR4 and CD14 trafficking and its influence on LPS-induced pro-inflammatory signaling. *Cell Mol Life Sci*. 2021;78(4):1233–1261. doi:10.1007/s00018-020-03656-y

69. Zhao G, Yu R, Deng J, et al. Pivotal role of reactive oxygen species in differential regulation of lipopolysaccharide-induced prostaglandins production in macrophages. *Mol Pharmacol*. 2013;83(1):167–178. doi:10.1124/mol.112.080762

70. Castaneda OA, Lee S-C, Ho C-T, Huang T-C. Macrophages in oxidative stress and models to evaluate the antioxidant function of dietary natural compounds. *J Food Drug Analysis*. 2017;25(1):111–118. doi:10.1016/j.jfda.2016.11.006

71. Vergallo C, Dini L, Szamosvölgyi Z, et al. In vitro analysis of the anti-inflammatory effect of inhomogeneous static magnetic field-exposure on human macrophages and lymphocytes. *PLoS One*. 2013;8(8):e72374. doi:10.1371/journal.pone.0072374

72. Madel M-B, Ibáñez L, Wakkach A, et al. Immune function and diversity of osteoclasts in normal and pathological conditions. *Front Immunol*. 2019;10. doi:10.3389/fimmu.2019.01408.

73. Xue Q, Yan Y, Zhang R, Xiong H. Regulation of iNOS on immune cells and its role in diseases. *Int J Mol Sci*. 2018;19(12). doi:10.3390/ijms19123805

74. Kawane T, Qin X, Jiang Q, et al. Runx2 is required for the proliferation of osteoblast progenitors and induces proliferation by regulating Fgfr2 and Fgfr3. *Sci Rep*. 2018;8(1):13551. doi:10.1038/s41598-018-31853-0

75. Bailey S, Karsenty G, Gundberg C, Vashishth D. Osteocalcin and osteopontin influence bone morphology and mechanical properties. *Ann N Y Acad Sci*. 2017;1409(1):79–84. doi:10.1111/nyas.13470

76. Si J, Wang C, Zhang D, Wang B, Hou W, Zhou Y. Osteopontin in bone metabolism and bone diseases. *Med Sci Monit*. 2020;26. doi:10.12659/MSM.919159